ISSN 0915-633X

NATIONAL INSTITUTE FOR FUSION SCIENCE

Global Mode Analysis of Ideal MHD Modes in a Heliotron/Torsatron System: I. Mercier-unstable Equilibria

J. Chen, N. Nakajima and M. Okamoto

(Received - Nov. 13, 1998)

NIFS-580 Dec. 1998

RESEARCH REPORT
NIFS Series

NAGOYA, JAPAN

Global mode analysis of ideal MHD modes in a heliotron/torsatron system: I. Mercier-unstable equilibria

J. Chen*, N. Nakajima†*, and M. Okamoto†*

†*National Institute for Fusion Science, Toki 509-5292, Japan;*

**Graduate University for Advanced Studies, Japan*

Abstract

By means of a global mode analysis of ideal MHD modes for Mercier-unstable equilibria in a planar axis $L = 2/M = 10$ heliotron/torsatron system with an inherently large Shafranov shift, the conjecture from local mode analysis for Mercier-unstable equilibria given in [N. Nakajima, Phys. Plasmas **3**, 4556 (1996)] has been confirmed and the properties of pressure-driven modes, namely, ballooning modes and interchange modes, inherent to such three-dimensional systems have been clarified. The change of the local magnetic shear due to the Shafranov shift, which is related to toroidicity, reduces the field line bending stabilizing effects on ballooning modes. According to the degree of the reduction of the local magnetic shear by the Shafranov shift, the Mercier-unstable equilibria are categorized into toroidicity-dominant (strong reduction) and helicity-dominant (weak reduction) Mercier-unstable equilibria. Since the local magnetic curvature due to helicity has the same period M in the toroidal direction as the toroidal field period of the equilibria, the characteristics of the pressure-driven modes in such Mercier-unstable equilibria dramatically change, both according to the reduction of the local magnetic shear by the Shafranov shift and also according to the relative magnitude of the typical toroidal mode number n of the perturbation compared with the toroidal field period of the equilibria M. In the toroidicity-dominant Mercier-unstable equilibria, the pressure-driven modes change from interchange modes for low toroidal mode numbers $n < M$, to tokamak-like poloidally localized ballooning modes with a weak toroidal mode coupling for moderate toroidal mode numbers $n \sim M$, and finally to both poloidally and toroidally localized ballooning modes purely inherent to three-dimensional systems for fairly high toroidal mode numbers $n \gg M$. In the helicity-dominant Mercier-unstable equilibria, the pressure-driven modes change from interchange modes for $n < M$ or $n \sim M$, directly to both poloidally and toroidally localized ballooning modes purely inherent to three-dimensional systems for $n \gg M$. Those interchange modes are localized on the inner side of the torus, because the Shafranov shift enhances the unfavorable magnetic curvature there rather than on the outer side of the torus. In both types of Mercier-unstable equilibria, the pressure driven modes become more unstable and more localized both on flux tubes and in the radial direction, and have stronger toroidal mode coupling through the magnetic curvature due to helicity, as the typical toroidal mode numbers increase. All of these properties are consistent with the conjecture from the local mode analysis.

Keywords: global mode analysis, toroidicity-dominant Mercier-unstable equilibrium, helicity-dominant Mercier-unstable equilibrium, interchange mode, tokamak-like ballooning mode, ballooning mode inherent to three-dimensional system.

I. INTRODUCTION

Previously, from an analysis of finite-β Magnetohydrodynamic (MHD) equilibria (where β is the ratio of the kinetic pressure to the magnetic pressure) in an $L = 2/M = 10$ planar axis heliotron/torsatron system with an inherently large Shafranov shift (where L and M are the polarity and toroidal field period of the helical coils, respectively), it has been shown that:

1. The local magnetic shear (which makes a stabilizing term for high-mode-number ballooning modes) is related to helicity of the helical coils in the considered vacuum configuration. Its change due to a large Shafranov shift is essentially axisymmetric, i.e., related to toroidicity. This change leads to the disappearance of the (integrated) local magnetic shear on the outer side of the torus, even in the region with a stellarator-like global magnetic shear, resulting in the destabilization of high-mode-number ballooning modes.[1]

2. The local normal magnetic curvature (which constructs a potentially destabilizing term for high-mode-number ballooning modes together with the pressure gradient) consists of parts due to both toroidicity and helicity of the helical coils, which determines the three-dimensional properties of the high-mode-number ballooning modes.[2]

In three-dimensional MHD equilibria, the eigenvalues ω^2 for high-mode-number ballooning modes have the functional form $\omega^2 = \omega^2(\psi, \theta_k, \alpha)$ where ψ labels the flux surface, α labels the magnetic field line on it, and θ_k is the radial wave number associated with the eikonal approximation. Since ω^2 has no α-dependence in axisymmetric systems, the stronger the α-dependence of ω^2 is (mainly coming from the helicity part of the local magnetic curvature), the more significant the three-dimensional properties of ω^2 are. The topological properties of the unstable eigenvalues ω^2 (< 0) in (ψ, θ_k, α) space, as schematically shown in Fig. 1, are the following[2]:

1. For Mercier-unstable equilibria, two types of topological level surfaces for ω^2 coexist in (ψ, θ_k, α) space. One is a tokamak-like topologically cylindrical level surface whose axis is in α direction. The other is a topologically spheroidal level surface inherent to three-dimensional systems, which is surrounded by the topologically cylindrical level surface. From the relative positional relation of these two types of level surfaces, modes with spheroidal level surfaces for ω^2 have larger growth rates than those with cylindrical level surfaces.

2. In Mercier-stable equilibria, only a topologically spheroidal level surface exists, which is surrounded by the level surfaces of stable Toroidicity-induced Alfvén Eigenmodes (TAE).

From these results, it was previously conjectured[2] that the global structure of pressure-driven modes would have the following properties:

1. Global modes that correspond to modes in the local mode analysis with a topologically cylindrical level surface for ω^2 will be poloidally localized tokamak-like ballooning modes or interchange modes. Effects of the toroidal mode coupling on these modes are weak.

2. Global modes corresponding to modes in the local mode analysis with a topologically spheroidal level surface for ω^2 will be such ballooning modes inherent to three-dimensional systems with strong toroidal mode coupling that they have high poloidal and toroidal mode numbers and are localized in both the poloidal and toroidal directions. These modes become localized within each toroidal field period of the heli-

cal coils, as their typical toroidal mode numbers become higher.

3. For Mercier-unstable equilibria, where both topologically cylindrical and spheroidal level surfaces for ω^2 coexist, poloidally localized tokamak-like ballooning modes or interchange modes with weak toroidal mode coupling appear when their typical toroidal mode numbers are relatively low. As the typical toroidal mode numbers become higher, such ballooning modes inherent to three-dimensional systems appear with strong toroidal mode coupling that they have larger growth rates and are localized in both the poloidal and toroidal directions, which lead to modes localized within each toroidal field period of the helical coils.

4. In Mercier-stable equilibria, where only a topologically spheroidal level surface for ω^2 exists, only such ballooning modes inherent to three-dimensional systems appear with strong toroidal mode coupling that they have high poloidal and toroidal mode numbers and are localized in both the poloidal and toroidal directions. These modes become localized within each toroidal field period of the helical coils, as their typical toroidal mode numbers become higher.

The purposes of the present work are to prove the above conjecture that was based on local mode analysis for Mercier-unstable equilibria and to clarify the inherent properties of pressure-driven modes, namely, ballooning and interchange modes, through a global mode analysis of the ideal MHD stability for Mercier-unstable equilibria in the planar axis $L = 2/M = 10$ heliotron/torsatron system used in Refs. 1 and 2.

The present paper is organized as follows. In Sec. II, the characteristics are given for the Mercier-unstable equilibria used in the global mode analysis of ideal MHD stability. In particular, we categorize Mercier-unstable equilibria into two types, viz., toroidicity-dominant Mercier-unstable equilibria and helicity-dominant Mercier-unstable equilibria. This categorization comes from the local properties of the Mercier-unstable equilibria brought by the Shafranov shift. The Shafranov shift in the considered planar axis three-dimensional system is essentially axisymmetric, namely, related to toroidicity, and hence the change of the local magnetic shear due to the Shafranov shift is also essentially related to toroidicity. As the Shafranov shift becomes larger, the field line bending stabilizing term due to the local magnetic shear is reduced, finally resulting in the destabilization of high-mode-number ballooning modes. The toroidicity-dominant Mercier-unstable equilibria are characterized by properties that it is easy for the local magnetic shear to vanish on the outer side of the torus, which is brought by a relatively large Shafranov shift. Thus, in the toroidicity-dominant Mercier-unstable equilibria, ballooning modes are easy to destabilize. The helicity-dominant Mercier-unstable equilibria are characterized by properties that it is hard for the local magnetic shear to vanish on the outer side of the torus, which is brought by a relatively small Shafranov shift. Thus, in the helicity-dominant Mercier-unstable equilibria, ballooning modes are difficult to destabilize. Note that, in both types of equilibria, the Shafranov shift locally reduces (enhances) the unfavorable normal magnetic curvature on the outside (inside) of the torus, which is another local property due to the Shafranov shift. The global mode analysis of pressure-driven modes is described in Sec. III. First, the numerical procedure for the global stability calculations is described. Then the results for the global mode analyses for toroidicity-dominant and helicity-dominant Mercier-unstable equilibria are presented. We find that the characteristics of the pressure-driven modes in such Mercier-unstable equilibria dramatically change, both according to the degree of the reduction of the field line bending stabilizing term by the Shafranov shift (according to the type of the Mercier-unstable equilibria) and also according

to the relative magnitude of the typical toroidal mode numbers n compared with the toroidal field period of the equilibria M. In the toroidicity-dominant Mercier-unstable equilibria, the relatively large Shafranov shift strongly reduces the stabilizing effects of the local magnetic shear on ballooning modes, so that tokamak-like poloidally localized ballooning modes occur from the moderate toroidal mode numbers $n \sim M$ following interchange modes with low toroidal mode numbers $n < M$. Both poloidally and toroidally localized ballooning modes inherent to three-dimensional MHD equilibria occur for fairly high toroidal mode numbers $n \gg M$. In contrast, in the helicity-dominant Mercier-unstable equilibria, the reduction of the stabilizing effects by the Shafranov shift is weak, and hence interchange modes occur for both low toroidal mode numbers $n < M$ and moderate toroidal mode numbers $n \sim M$. For fairly high toroidal mode numbers $n \gg M$, just as for the toroidicity-dominant Mercier-unstable equilibria, ballooning modes inherent to three-dimensional MHD equilibria occur. All of these properties of the pressure-driven modes in Mercier-unstable equilibria are quite consistent with the conjecture from local mode analysis given in Ref. 2. In both types of equilibria, interchange modes have a radially extended structure on the inside of the torus, which comes from the change of the local normal magnetic curvature due to the Shafranov shift. The conclusion and discussioin are given in Sec. IV.

II. PROPERTIES OF MERCIER-UNSTABLE EQUILIBRIA

As the vacuum configuration, we use an $L = 2/M = 10$ planar axis heliotron/torsatron configuration like that for the Large Helical Device[4] (LHD). This configuration is exactly the same as that used in Refs. 1 and 2. The three-dimensional finite-β equilibria are calculated with the Variational Moment Equilibrium Code[5] (VMEC) under the condition of a fixed boundary. The boundary is determined from the outermost flux surface of the vacuum magnetic field, which has nearly concentric circular magnetic flux surfaces when averaged in the toroidal direction. The properties of the vacuum configuration are understood as a straight helical configuration toroidally bended. Since the aspect ratio is relatively high: $R_0/a = 7 \sim 8$ [here R_0 and a are the major and minor radii, respectively], the global and local properties of the vacuum configuration are mainly determined by helicity of the helical coils. As global properties, surface quantities – namely, the global rotational transform ι, the global magnetic shear $s \equiv 2d\ln\iota/d\ln\psi$, the quantity $d^2V/d\psi_N^2$ that measures the average favorable magnetic curvature (average magnetic well) [$d^2V/d\psi_N^2 < 0$ means an average favorable magnetic curvature], and the Mercier criterion parameter D_M [$D_M > 0$ means Mercier stable, for the definition see Eq. (3) in Ref. 2] are drawn in Fig. 2 as functions of the normalized radial coordinate $r_N \equiv \sqrt{\psi_N}$, where $\psi_N = \psi/\psi_{edge}$ is the normalized toroidal flux, and ψ is the label of the flux surface, defined as $\psi = \Phi_t/(2\pi)$ with Φ_t the toroidal flux inside a flux surface. The stellarator-like global magnetic shear s (> 0) and the average unfavorable magnetic curvature (magnetic hill): $d^2V/d\psi_N^2 > 0$ are shown in the whole plasma region, just as in a corresponding straight helical system. As well as the global quantities, the local quantities associated with the high-mode-number ballooning mode analysis (local mode analysis), namely, the local magnetic shear and the local magnetic curvature are strongly related to helicity in the vacuum configuration. In order to express such local quantities, the Boozer coordinate system[6] (ψ, θ, ζ) is used, with ψ the radial coordinate, and θ and ζ the poloidal and toroidal angles, respectively. The origin for the poloidal angle θ is on the outer side of the torus and the origin for the toroidal angle is on the vertically elongated poloidal cross sec-

tion. The local magnetic shear $\hat{s}$ is decomposed into the global magnetic shear s and the oscillatory part $\tilde{s}$ as

$$\hat{s} = \frac{2\psi\sqrt{g}}{\epsilon}\vec{s}\cdot\nabla\times\vec{s} = s+\tilde{s}, \quad \vec{s} = \frac{\nabla\psi\times\vec{B}}{|\nabla\psi|^2}, \quad (1)$$

with

$$s = 2\frac{d\ln\epsilon}{d\ln\psi}, \quad \tilde{s} = \left(\frac{1}{\epsilon}\frac{\partial}{\partial\zeta}+\frac{\partial}{\partial\theta}\right)\left[\frac{2\psi(Jg_{\psi\theta}-Ig_{\psi\zeta})}{\sqrt{g}|\nabla\psi|^2}\right], \quad (2)$$

where $2\pi J$ is the poloidal current outside a flux surface and $2\pi I$ is the toroidal current inside, and the covariant metrics are given by $g_{\psi\theta} = \partial_\psi\vec{r}\cdot\partial_\theta\vec{r}$ and $g_{\psi\zeta} = \partial_\psi\vec{r}\cdot\partial_\zeta\vec{r}$. The magnetic curvature $\vec{\kappa}$ is also decomposed into the normal magnetic curvature κ^n and the geodesic magnetic curvature κ_g as

$$\vec{\kappa} \equiv (\hat{n}\cdot\nabla)\hat{n} = \kappa^n\frac{\nabla\psi}{2\psi}+\kappa_g\vec{s}. \quad (3)$$

where $\hat{n}\equiv\vec{B}/B$ is the unit vector along a magnetic field line and

$$\kappa^n = \frac{2\psi}{|\nabla\psi|^2}\vec{\kappa}\cdot\nabla\psi = \frac{2\psi}{B^2|\nabla\psi|^2}\nabla\psi\cdot\nabla\left(P+\frac{B^2}{2}\right), \quad (4)$$

$$\kappa_g = \frac{|\nabla\psi|^2}{B^2}\vec{\kappa}\cdot\vec{s} = \frac{1}{2}\vec{B}\times\nabla\psi\cdot\nabla\left(\frac{1}{B^2}\right). \quad (5)$$

The local magnetic shear $\hat{s}$ and the normal and geodesic magnetic curvatures, κ^n and κ_g, appear in the high-mode-number ballooning equation in the covering space (ψ,η,α) [here $\eta=\theta$, and $\alpha=\zeta-\theta/\epsilon$, $(-\infty<\eta<+\infty,\ 0\le\alpha\le 2\pi/M)$]:[2]

$$\frac{\partial}{\partial\eta}\left[|\vec{k}_\perp|^2\frac{\partial}{\partial\eta}\Phi\right]+\Omega^2\left(\frac{\langle B^2\rangle}{B^2}\right)^2|\vec{k}_\perp|^2\Phi + \frac{2}{B_0}\frac{J+\epsilon I}{\epsilon^2}\sqrt{g}\frac{dP}{d\psi}\left[\kappa^n-\kappa_g\int^\eta\hat{s}d\eta\right]\Phi=0, \quad (6)$$

where $|\vec{k}_\perp|$ is the perpendicular wave number including the local magnetic shear integrated along a magnetic field line, which is given by

$$|\vec{k}_\perp|^2 = \frac{|\nabla\psi|^2}{2\psi B_0}\left[\left(\frac{2\psi B}{|\nabla\psi|^2}\right)^2+\left[\int^\eta\hat{s}d\eta\right]^2\right]. \quad (7)$$

and $\Omega = \omega\tau_A$ is the eigenfrequency normalized by the Alfvén time τ_A, which is given by $\tau_A^2 = \rho_m/\left(2\pi\epsilon d\Phi_I/d\Psi\right)^2$. The integrated local magnetic shear along a magnetic field line $\int\hat{s}d\eta$ contributes to both the first and second stability of high-mode-number ballooning modes as a stabilizing term. The unfavorable normal magnetic curvature κ^n contributes to the first stability of high-mode-number ballooning modes as a destabilizing term. The geodesic magnetic curvature κ_g contributes to the first and second stability together with the integrated local magnetic shear along a magnetic field line $\int\hat{s}d\eta$. In the following global mode analysis of the ideal MHD stability, we could not appreciate the significant influences of the geodesic magnetic curvature on pressure-driven modes, and hence we concentrate our attention on the local magnetic shear $\hat{s}$ and the normal magnetic curvature κ^n. Shown in Fig. 3 are equally spaced (ψ,θ) meshes [Figs. 3(a)] and the corresponding contours for the local magnetic shear $\hat{s}$ [Figs. 3(b)], and for the normal magnetic curvature multiplied by the Jacobian $\sqrt{g}\kappa^n$ [Figs. 3(c)]; these are shown both on vertically (left column) and horizontally (right column) elongated poloidal cross sections. It is shown in Fig. 3 that the local properties of the local magnetic shear and the normal magnetic curvature mainly come from helicity in the vacuum configuration. The effect of toroidicity is more apparent in the normal magnetic curvature $\sqrt{g}\kappa^n$ than in the local magnetic shear $\hat{s}$. On the horizontally elongated poloidal cross section, the locally unfavorable magnetic curvature due to helicity is superposed on that due to toroidicity on the outer side of the torus, and hence the normal magnetic curvature is more unfavorable on the outer side of the torus than on the inner side of the torus. In contrast, on the vertically elongated poloidal cross section, the locally favorable magnetic curvature due to helicity cancels the locally unfavorable magnetic curvature due to toroidicity, leading to locally favorable magnetic curvature even on the outer side of the torus.

The properties of the finite-β equilibria are basically understood as a modification of the vacuum configuration by an essentially axisymmetric and inherently large Shafranov shift. The essential structure of the Shafranov shift is understood by a model equation. With the use of the stellarator expansion with high-β ordering – viz., $\beta \sim O(\varepsilon_t)$, $\varepsilon_t = a/R_0$ – a model expression for the Shafranov shift Δ is found as[1]

$$\frac{d\Delta}{dr} = \frac{R_0}{4\iota^2}\frac{d\beta}{dr} \sim O(1) \tag{8}$$

where r is the radial coordinate, $\beta = 2P/B_0^2$, and B_0 is the magnetic field strength at $R = R_0$. From Eq.(8), it is found that either peaked pressure profiles with no net toroidal current or peaked pressure profiles with a net toroidal current making ι decrease create a large Shafranov shift. In contrast, for the same beta value β_0 at the magnetic axis, broad pressure profiles with no net toroidal current or broad pressure profiles with a net toroidal current making ι increase create small Shafranov shift. Since the properties of the vacuum configuration is mainly determined by helicity as shown in Fig. 3 and since the Shafranov shift is essentially axisymmetric, the larger the Shafranov shift becomes, the more significant the effects by toroidicity become, compared with helicity. Such a Shafranov shift changes the local and global properties of equilibria,[1,2] namely, the reduction of the local magnetic shear (local property) and the formation of the average favorable normal magnetic curvature near the magnetic axis (global property). The former is unfavorable to ballooning modes through the reduction of the field line bending stabilizing effects and the latter is favorable to interchange modes through the Mercier criterion D_M. Since only Mercier-unstable equilibria are considered, according to the reduction of the local magnetic shear brought by the Shafranov shift, Mercier-unstable equilibria can be categorized into two types, namely, toroidicity-dominant Mercier-unstable equilibria and helicity-dominant Mercier-unstable equilibria. The toroidicity-dominant Mercier-unstable equilibria are created by a relatively large Shafranov shift. These equilibria are characterized by local properties that the (integrated) local magnetic shear is strongly reduced by the Shafranov shift, leading to the situation that ballooning modes would be easy to destabilize. In contrast, the helicity-dominant Mercier-unstable equilibria are created by a relatively small Shafranov shift. These equilibria are characterized by local properties that the (integrated) local magnetic shear is not reduced so much by the Shafranov shift, leading to the situation that ballooning modes would be difficult to destabilize.

On the basis of these considerations, in this paper the following two types of Mercier-unstable equilibria have been adopted in order to examine the competitive or synergetic effects of toroidicity and helicity on pressure-driven modes. The toroidicity-dominant Mercier-unstable equilibrium is created with the peaked pressure profile $P = P_0(1 - \psi_N)^2$ with $\beta_0 = 5.9\%$, under the flux conserving condition, i.e., with a specified profile for the rotational transform ι. Note that this equilibrium is slightly more Mercier unstable than one with the same pressure profile but no net toroidal current, made by specifying ι to be larger than that obtained under the zero-current condition. The toroidicity-dominant Mercier-unstable equilibrium with the same pressure profile under the currentless condition are now under investigation, associated with Mercier-stable equilibria. The helicity-dominant Mercier-unstable equilibrium is created with the broad pressure profile $P = P_0(1 - \psi_N^2)^2$ and $\beta_0 = 4.0\%$, under the currentless condition. Note that this equilibrium is exactly the same as used in Ref. 2. In order to show the global properties, surface quantities are drawn in Fig. 2 as functions of the normalized radial coordinate $r_N \equiv \sqrt{\psi_N}$ for both the toroidicity-dominant [Fig. 2(a)] and helicity-dominant [Fig. 2(b)] Mercier-unstable equilibria. The helicity-dominant equilibrium with the broad pressure profile is rather Mercier

unstable, compared with the toroidicity-dominant equilibrium.

Shown in Fig. 4 are equally spaced (v, θ) meshes [Figs. 4(a)] and the corresponding contours for the local magnetic shear $\hat{s}$ [Figs. 4(b)], and for the normal magnetic curvature multiplied by the Jacobian $\sqrt{g}\kappa^n$ [Figs. 4(c)] both on vertically (left column) and horizontally (right column) elongated poloidal cross sections for the toroidicity-dominant Mercier-unstable MHD equilibrium. Same quantities are drawn in Fig. 5 for the helicity-dominant Mercier-unstable MHD equilibrium. A comparison of Figs. 3(b), 4(b), and 5(b) indicates that the local magnetic shear, which is the stabilizing term of high-mode-number ballooning modes, is significantly reduced on the outer side of the torus, especially at the horizontally elongated poloidal cross section, as the Shafranov shift increases. Moreover, it is understood from a comparison of Figs. 3(c), 4(c), and 5(c) that the locally unfavorable magnetic curvature at the horizontally elongated poloidal cross section becomes stronger on the inner side of the torus than that on the outer side of the torus. The reason is as follows. In this horizontally elongated poloidal cross section, the normal magnetic curvature κ^n is approximated as

$$\kappa^n = \frac{v}{B^2}\frac{\partial B^2}{\partial v}. \qquad (9)$$

At the considered β-value, the diamagnetic effect is so weak that the distribution of the magnetic field strength hardly changes. However, the change in the distribution of flux surfaces due to the Shafranov shift is quite large as shown in Figs. 4(a) and 5(a). The interval of flux surfaces on the inner side of the torus is wider than that on the outer side of the torus. Therefore, the locally unfavorable magnetic curvature at the horizontally elongated poloidal cross section becomes stronger on the inner side of the torus than that on the outer side of the torus.

It would be worthwhile mentioning the followings. As β increases, the toroidicity-dominant Mercier-unstable equilibria created by peaked pressure profiles with no net toroidal current have a second stability region with respect to interchange modes. The reason is that the average magnetic curvature due to the Shafranov shift is favorable in the region where the maximum pressure gradient of peaked pressure profiles exists. In contrast, helicity-dominant Mercier-unstable equilibria created by broad pressure profiles with no net toroidal current do not have second stability against interchange modes, because the maximum pressure gradient still exists in an average unfavorable magnetic curvature region. Thus, the toroidicity-dominant equilibria are more Mercier stable than the helicity-dominant equilibria.

III. GLOBAL MODE ANALYSIS OF PRESSURE-DRIVEN MODES

A. Numerical procedure

For the global mode analysis of ideal MHD stability, we used a version of the Code for the Analysis of the MHD Stability of 3-Dimensional equilibrium (CAS3D): namely, the CAS3D2MN version[7,8], which is based on a formulation of the ideal MHD energy principle in the Boozer coordinate system (v, θ, ζ) and in which the finite-element-Fourier method is used. Here, we address four important points concerning global mode analysis with the use of the CAS3D2MN code.

1. Fourier space of the equilibria[7]

The three-dimensional equilibrium is expressed in terms of the Fourier decomposition in both the poloidal and toroidal directions. Let m_e and n_e be the poloidal and toroidal mode numbers of the equilibrium, respectively. In the following calculations, 31 poloidal modes ($0 \le m_e \le 30$) and 21 toroidal

modes ($-10 \leq n_e/M \leq +10$. where M is the toroidal field period of the equilibria, with $M = 10$) are used to express the three-dimensional equilibria. Therefore, the total number of Fourier modes M_{eq} is 641. The accuracy of the mapping from VMEC coordinates to Boozer coordinates is estimated from the relative errors in B and R due to the transformation at the grid points. The maximum relative errors in B and R for the toroidicity-dominant equilibrium are 1×10^{-5} and 3×10^{-7}, respectively. For the helicity-dominant equilibrium, the corresponding relative errors are 7×10^{-7} and 1×10^{-7}. Note that the number of poloidal modes is important for equilibria with a large Shafranov shift, in order to be able to reconstruct the MHD equilibrium in the Boozer coordinate system, and that this number increases as the Shafranov shift becomes larger.

2. Fourier space of the perturbations[7]

The phase factor (M_p, N_p) has been introduced in order to select Fourier modes (m, n) of the perturbation in the desired Fourier space and to reduce the memory and CPU time. For example, the normal displacement $\vec{\xi} \cdot \nabla \psi$ is expressed in the following manner (where the notations are slightly different from those in Refs. 7 and 8 for convenience)

$$\vec{\xi} \cdot \nabla \psi = X^e \cos[M_p \theta - N_p \zeta] + Y^o \sin[M_p \theta - N_p \zeta]. \tag{10}$$

where

$$\begin{aligned} X^e &\equiv \sum_{i=1}^{M^*_{eq}} \hat{X}^e_i(\psi_N) \cos[m_e(i)\theta - n_e(i)\zeta]. \\ & \quad M^*_{eq} \leq M_{eq}, \\ Y^o &\equiv \sum_{i=1}^{M^*_{eq}} \hat{Y}^o_i(\psi_N) \sin[m_e(i)\theta - n_e(i)\zeta]. \end{aligned} \tag{11}$$

In Eq. (11), M^*_{eq} is the total number of Fourier modes selected from the Fourier space of the equilibrium. Thus, a Fourier mode (m, n) of the perturbation is expressed as a combination between the Fourier mode of the equilibrium (m_e, n_e) and the phase factor (M_p, N_p):

$$\begin{aligned} m &= M_p + m_e(i), \; n = N_p + n_e(i), \quad i = 1, \cdots, M^*_{eq} \\ m &= M_p - m_e(i), \; n = N_p - n_e(i). \end{aligned} \tag{12}$$

Thus, the total number of Fourier modes of the perturbation is $M_{pt} = 2M^*_{eq} - 1$. Both the phase factor (M_p, N_p) and Fourier modes of the equilibrium (m_e, n_e) to the number of M^*_{eq} are carefully chosen, in order that a set of the Fourier modes (m, n) of the perturbation is selected in a desired Fourier sub-space around (M_p, N_p).

Figure 6(a) shows the chosen Fourier modes (m_e, n_e) denoted by plus signs ($M^*_{eq} = 186$) and the Fourier space of the equilibrium indicated by the rectangular box, and Fig. 6(b) shows the resultant Fourier modes (m, n) of the perturbation with the phase factor $(M_p, N_p) = (38, 22)$. Hence we have $M_{pt} = 2M^*_{eq} - 1 = 371$. These values are used for the stability calculations, with the typical toroidal mode number of the perturbation being $n \sim M$. The same quantities are displayed in Fig. 7 for $M^*_{eq} = 336$ and $(M_p, N_p) = (133, 77)$, so that $M_{pt} = 2M^*_{eq} - 1 = 671$; these were used for the stability calculations when the typical toroidal mode number of the perturbation is $n \gg M$.

From this procedure to construct the Fourier modes of the perturbation, it is noted that a sufficiently large Fourier space of the equilibrium is needed in order to express ballooning modes that consist of the superposition of many resonant Fourier modes. An especially large number of poloidal modes is required in equilibria that have strong global magnetic shear. We also note that this phase factor technique is particularly powerful for the analysis of short-wave-length perturbations.

3. Radial interval[7]

By knowing the radial localization of a particular perturbation, we are able to reduce the radial range

of the equilibrium while still keeping sufficient radial resolution. The radial direction is spanned by N_S+1 radial grid points, with $\Delta S \equiv 1/N_S$ the radial resolution. When the region where the perturbation localizes is roughly known – say, from v_{Ns} (> 0) to v_{Ne} (< 1) – the stability calculations are limited in the range $[v_N] = [v_{Ns}, v_{Ne}]$, with the boundary condition $\vec{\xi} \cdot \nabla v = 0$ at both end points. This technique is especially powerful for the analysis of short-wave-length perturbations in equilibria with strong global magnetic shear. In the following calculations, v_{Ns} (> 0) and v_{Ne} (< 1) are used in order to effectively reduce the radial region for short-wave-length perturbations and also to reduce the needed memory and CPU time. This also avoids equilibrium numerical errors near the magnetic axis and the boundary, if any such errors exist in the calculated equilibrium.

4. Shift-and-invert Lanczos algorithm[9]

The most difficult part of a global mode analysis is to solve the eigenvalue problem of a real symmetric band matrix A with the order $dim(A)$ of $\sim 10^6$. Consequently, the shift-and-invert Lanczos algorithm is employed. The Lanczos algorithm can focus on a desired portion of the spectrum by reducing the original matrix A to a Lanczos matrix T_m whose order is much smaller than that of A, namely, $dim(T_m) \ll dim(A)$. The main arithmetic operations come from $A\vec{q}$ where $\vec{q}$ is a Lanczos vector. Therefore, parallelization can be easily done and also extra memory requirements can be controlled to be negligible.

The application is performed as follows: (1) Make A a positive definite matrix C with the use of an appropriate shift of the eigenvalue $\delta\lambda$. (2) Calculate a desired portion of the spectrum of the inverse matrix of C with the Lanczos algorithm. (3) Check the convergence between the eigenvalues from the Lanczos matrix and those of the original matrix. If the convergence is not good, the procedures from (2) to (3) are repeated until convergence is satisfied. (4) Transform the eigenvalues so obtained into ones of the original matrix by taking account of $\delta\lambda$. As the input parameters, we need to specify the maximum relative error between the eigenvalues of the Lanczos matrix and those of the original matrix, namely, the convergence tolerance ε; the order of the Lanczos matrix in the initial step $dim(T_0)$; and the shift of the eigenvalue $\delta\lambda$. The order of the Lanczos matrix $dim(T_m)$ is automatically increased in order to satisfy convergence tolerance. In the following calculations, the typical values of $\varepsilon = 1.0 \times 10^{-5}$, $dim(T_0) = 100$, and $\delta\lambda = 0.1$ are used. For well convergent cases, $dim(T_m) = 200$ is enough for convergence; however, $dim(T_m) = 1000$ is needed for badly convergent cases. When the order of the matrix for global mode analysis of three-dimensional equilibria is very large (say, 10^6), we note that the shift-and-invert Lanczos algorithm is very powerful.

B. Global mode analysis for toroidicity-dominant Mercier-unstable equilibrium

Pressure-driven modes with long-wave-lengths – e.g., long-wave-length interchange modes – experience the magnetic curvature with its local variation averaged out. As the wave length becomes shorter, pressure-driven modes begin to feel the local structure of the magnetic curvature. The three-dimensional equilibria considered here have toroidal field period M, and this is what mainly determines the toroidal period of the local magnetic curvature due to helicity. Therefore, we investigate the properties of pressure-driven modes for various cases of relative magnitude between the typical toroidal mode number of the perturbation, n, and the toroidal period of the local magnetic curvature due to helicity, M: namely, $n < M$, $n \sim M$, and $n \gg M$. For a particular selection of the numerical parameters, namely, the Fourier modes of the perturbation, the radial resolution, and the radial interval, there are

many unstable eigenvalues. In the followings, we will examine the most unstable eigenmodes for a particular selection of the numerical parameters.

For low toroidal mode numbers $n < M$, interchange modes occur, which feel the average magnetic curvature with its local variation averaged out. One of them is shown in Fig. 8. The radial distribution of the Fourier components of the normal displacement $\vec{\xi} \cdot \nabla\psi$ is shown in Fig. 8(a). Three resonant mode structures with $n = 3$ are visible, whereas the amplitudes of other modes with different toroidal mode numbers are quite small, and hence the toroidal mode coupling is negligible. This toroidicity-dominant equilibrium is weakly Mercier unstable as shown in Fig. 2(a), and the dominant mode with $(m, n) = (5, 3)$ is quite radially localized around the resonant surface with $\iota = 3/5$ in the Mercier-unstable region with $D_M < 0$, together with two small resonant structures at $\iota = 3/6$ and $\iota = 3/4$, both of which are slightly outside the Mercier-unstable region. The corresponding contours of the perturbed pressure $\tilde{P} = -\nabla P \cdot \vec{\xi}$ on both vertically and horizontally elongated poloidal cross sections are shown in Figs. 8(b) and (c). Comparison of the direction between magnetic field lines and constant level surfaces of $\tilde{P} = -\nabla P \cdot \vec{\xi}$ shows that the amplitude of the perturbation is almost constant along a magnetic field line. From these properties, it is concluded that this perturbation is an interchange mode almost free from the toroidal mode coupling. These interchange modes more radially extend on the inner side of the torus than on the outer side of the torus, which is difficult, however, to understand from Fig. 8. The detail of the mode structure of the interchange modes will be discussed in the next sub-section.

For moderate toroidal mode numbers $n \sim M$, the modes begin to feel the local structure of the magnetic curvature due to helicity. Since the Shafranov shift strongly reduces the stabilizing effects due to the local magnetic shear on the outer side of the torus in the toroidicity-dominant Mercier-unstable equilibrium as shown in Fig.4 (b), tokamak-like poloidally localized ballooning modes with weak toroidal mode coupling occur. This is shown in Fig. 9, where the Fourier space of the perturbation shown in Fig. 6 is used. The typical toroidal mode numbers are still so small that the modes can not feel the local structure of the magnetic curvature due to helicity effectively, and hence the toroidal mode coupling is weak. In Fig. 9(a), three groups of Fourier modes for the normal displacement $\vec{\xi} \cdot \nabla\psi$ with different toroidal mode numbers are visible, namely, $n = 22$, $n = 32$, and $n = 42$; these result from the weak toroidal mode coupling in the three-dimensional equilibrium. Each group, however, consists of many Fourier modes with different poloidal mode numbers caused by the poloidal mode coupling, and the Fourier modes existing in the region with a finite global magnetic shear ($r_N \geq 0.55$) have the largest amplitude around the resonant flux surface satisfying $\iota = n/m$. Thus, the structure of each group due to the poloidal mode coupling is quite similar to that of ballooning modes in tokamak plasmas. The Fourier modes have the finite amplitude in the region where the rotational transform monotonically increases in the radial direction ($r_N \geq 0.4$), as shown in Fig. 2(a), so that the group of Fourier modes with higher toroidal mode number appear in the outer flux surfaces. The most dominant group of the Fourier modes with $n = 32$ exists around the Mercier-unstable region, and other two groups with $n = 22$ and $n = 42$ extend from the Mercier-unstable region into the Mercier-stable region. The group with $n = 22$ extends into a considerably weak magnetic shear region ($r_N \sim 0.5$), where the high-mode-number ballooning formalism breaks down, and slightly off-resonant modes without the resonant surface have the finite amplitude there. Note that among the three groups of Fourier modes with different toroidal mode numbers, neighboring groups have opposite phase: e.g., between $n = 22$ and $n = 32$, and between $n = 32$ and $n = 42$. The relation between this relative phase difference

and the position of the origin of the toroidal angle, which is located where the poloidal cross section is vertically elongated, indicates a weak localization of the mode in the toroidal direction. A comparison of Figs. 9(b) and (c) shows that on the outer side of the torus, the radial extention of the perturbed pressure $\tilde{P} = -\nabla P \cdot \vec{\xi}$ is larger on the horizontally elongated poloidal cross section with locally unfavorable magnetic curvature at the outside of the torus, than on the vertically elongated poloidal cross section with locally favorable magnetic curvature at the outside of the torus. On the vertically elongated poloidal cross section, the perturbed pressure on the outer side of the torus changes phase in the radial direction.

For fairly high toroidal mode numbers $n \gg M$, the modes can easily distinguish the local fine structure of the magnetic curvature due to helicity. This results in the appearance of ballooning modes inherent to three-dimensional systems, which have such strong poloidal and toroidal mode couplings as to localize in both the poloidal and toroidal directions, as shown in Fig. 10, where a Fourier space for the perturbation larger than that in Fig. 7 is used, namely, $M_{eq}^{*} = 397$, $(M_p, N_p) = (342, 198)$, and $M_{pt} = 793$. There are eight groups of Fourier modes with different toroidal mode numbers for $\vec{\xi} \cdot \nabla \psi$ through the strong toroidal mode coupling. Their different toroidal mode numbers are shown in Fig. 10(a), namely, $n = 178, 188, 198, 208, 218, 228, 238$, and 248. All groups exist around Mercier-unstable region, where the rotational transform ι monotonically increases in the radial direction. The groups of Fourier modes with higher toroidal mode numbers exist in the region with higher rotational transform, and neighboring groups of Fourier modes have opposite phase to each other, just as in Fig. 9(a). This relative phase difference of the neighboring groups leads to the clear localization of the perturbed pressure in the toroidal direction, as shown in Figs. 10(b) and (c). On the outer side of the torus, the perturbed pressure, which localizes on the horizontally elongated poloidal cross section with the locally unfavorable magnetic curvature at the outside of the torus, almost disappears on the vertically elongated poloidal cross section with the locally favorable magnetic curvature at the outside of the torus. Moreover, the strong toroidal mode coupling causes a type of poloidal localization that is different from the kind only due to poloidal mode coupling. This phenomenon becomes quite clear in Fig. 10(d), which shows the corresponding contours of the perturbed pressure on the (θ, ζ) plane with one period in the poloidal direction and one-tenth of a period (one field period) in the toroidal direction at $r_N = 0.734$, where $\iota = 0.58$ which is where the Fourier mode with $n = 208$ has its maximum amplitude, as indicated in Fig. 10(a). In Fig. 10(d), it can be seen that regions where the perturbed pressure has large amplitude (indicated by dark diagonal stripes) alternate with regions of quite small amplitude (denoted by white diagonal stripes). Judging from the value of the rotational transform on this flux surface, namely, $\iota = 0.58$, we conclude that these high-amplitude and low-amplitude stripes are aligned along magnetic field lines, and that the strong toroidal mode coupling in addition to the poloidal mode coupling makes the perturbation be localized on selected flux tubes. The small amplitude regions (white diagonal stripes) also show that, as well as in the poloidal direction, there is a region with rather low amplitude in the toroidal direction on the outer side of the torus, around the vertically elongated poloidal cross section, namely, at $\theta \sim 0$ and $\zeta \sim 0$ (since the origins for the poloidal and toroidal angles exist on the outer side of the torus and on the vertically elongated poloidal cross section, respectively). In the case of a tokamak, these low-amplitude regions occur due only to the poloidal mode coupling, and consequently their widths are very narrow. The ballooning modes that are inherent to three-dimensional systems still have fairly extended structures in the toroidal direction, as shown in Fig. 10, and they do not localize in one toroidal field period.

Independent of the value for the typical toroidal mode numbers, unstable modes are radially localized near the Mercier-unstable region. As the typical toroidal mode numbers increase, the radial intervals, in which modes are localized, become more narrow and the modes become more unstable, and also the toroidal mode coupling becomes stronger through the normal magnetic curvature due to helicity. Therefore, it is expected that more unstable ballooning modes localized in one toroidal field period, which are conjectured in the local mode analysis[2], may occur in quite narrow radial intervals as the typical toroidal mode numbers become increasingly larger.

C. Global mode analysis for helicity-dominant Mercier-unstable equilibrium

For low toroidal mode numbers $n < M$, interchange modes occur, as shown in Fig. 11, just as in the case for the toroidicity-dominant equilibrium. The radial distribution of the Fourier components of the normal displacement $\vec{\xi}\cdot\nabla\psi$ is shown in Figs. 11(a) [where the origin of the poloidal angle is on the outer side of the torus] and (b) [where the origin of the poloidal angle is on the inner side of the torus], where three resonant mode structures with $n = 4$ are visible. The amplitudes of modes with different toroidal mode numbers are quite small. This equilibrium is quite Mercier unstable, as indicated in Fig. 2(b), so that the interchange mode has a fairly radially extended structure around the mode rational surfaces with $\epsilon = 4/7$, $4/6$, and $4/5$, all of which are inside the Mercier-unstable region with $D_M < 0$. The contours of the perturbed pressure $\tilde{P} = -\nabla P\cdot\vec{\xi}$ shown in Figs. 11(c) and (d) indicate that the interchange modes with $n < M$ have a large radial extension on the inner side of the torus and change phase in the radial direction on the outer side of the torus. This is because the normal magnetic curvature is more unfavorable on the inner side of the torus than on the outer side of the torus by the Shafranov shift as shown in Fig. 5(c) and also consistent with the results in Refs. 11 and 12. These properties are more easily understood from Fig. 11(b), where the Fourier modes of the normal displacement $\vec{\xi}\cdot\nabla\psi$ are displayed with the origin of the poloidal angle shifted from the outer side of the torus to the inner side of the torus, so that the Fourier components with an odd poloidal mode number change their signs. In this case, the Fourier modes with $(m, n) = (7, 4)$ and $(m, n) = (5, 4)$ change their signs. The mode structure is similar to that of a ballooning mode except that each Fourier mode has both positive and negative parts, which means that this type of interchange mode has a tendency to extend radially (or to localize) on the inner side of the torus and to change phase in the radial direction on the outer side of the torus through poloidal mode coupling. In other words, this type of interchange mode is anti-ballooning with respect to the poloidal mode coupling.

For moderate toroidal mode numbers $n \sim M$, Fig. 12 shows that interchange modes still occur, in which the Fourier modes of the perturbation shown in Fig. 6 are used, just as in Fig. 9. However, tokamak-like poloidally localized ballooning modes do not appear in the helicity-dominant Mercier-unstable equilibria, in contrast to the case for the toroidicity-dominant Mercier-unstable equilibrium shown in Fig. 9, because the reduction of the stabilizing term of ballooning modes by the Shafranov shift is not enough for tokamak-like poloidally localized ballooning modes to be destabilized as shown in Fig. 5(b). Thus, interchange modes driven by the average unfavorable magnetic curvature can be destabilized. The toroidal mode coupling of interchange modes becomes stronger as the toroidal mode number increases, as shown in Figs. 12(a) [where the origin of the poloidal angle is on the outer side of the torus] and (b) [where the origin of the poloidal angle is on the inner side of the torus], where two groups

of Fourier modes with $n = 22$, and $n = 32$ are dominant. Just as for interchange modes with $n < M$ shown in Fig. 11, the interchange modes with $n \sim M$ also have a tendency to be radially extended on the inner side of the torus and to change phase in the radial direction on the outer side of the torus due to poloidal mode coupling, as shown in Figs. 12(c) and (d). Moreover, the weak toroidal mode coupling, in cooperation with the poloidal mode coupling, causes a bumpy-like localization of the perturbed pressure in the poloidal direction, which is more clearly seen on the inner side of the torus in Figs. 12(c) and (d).

For fairly high toroidal mode numbers $n \gg M$, just as for the toroidicity-dominant Mercier-unstable equilibrium, the modes can distinguish the fine local structure of the magnetic curvature due to helicity. This results in ballooning modes inherent to three-dimensional systems just as for the toroidicity-dominant Mercier-unstable equilibrium shown in Fig. 10, which have strong poloidal and also toroidal mode couplings and localize in both the poloidal and toroidal directions, as shown in Fig. 13, where the Fourier modes of the perturbation shown in Fig. 7 are used. The dominant toroidal mode numbers of the Fourier modes of $\vec{\xi} \cdot \nabla \psi$ are shown in Fig. 13(a), namely, $n = 67, 77, 87, 97, 107, 117$, and 127. Although there are fewer than for the case of the ballooning mode shown in Fig. 10(a), a similar mode structure is obtained. The most dominant toroidal mode number of this ballooning mode, $n \sim 97$, is fairly small compared with the corresponding mode number, $n \sim 208$ in Fig. 10. Therefore, the degree of localization of the ballooning mode on the flux tubes is relatively weak, as can be seen in Figs. 13(b), (c), and (d).

Just as for toroidicity-dominant equilibria, unstable modes radially localize around the Mercier-unstable region independent of their typical toroidal mode numbers. As the typical toroidal mode numbers increase, the modes become more unstable and more radially localized, and have a stronger toroidal mode coupling through the normal magnetic curvature due to helicity. Compared to the interchange modes with low toroidal mode numbers shown in Fig. 11, interchange modes with moderate toroidal mode numbers (shown in Fig. 12) and ballooning modes with fairly high toroidal mode numbers (shown in Fig. 13) are significantly localized in the radial direction.

In order to investigate those results in Sec. III B and C more carefully, two different auxiliary equilibria were introduced, created by changing only the boundary shape of the original equilibria. One is a toroidicity-dominant equilibrium and the other is a helicity-dominant equilibrium. Both auxiliary equilibria have quite similar local structures of the local magnetic shear and the normal magnetic curvature to those in the original equilibria, and are more Mercier unstable than the original equilibria, as shown in Fig. 2 by the dashed curves. In spite of difference of the violated level of the Mercier criterion, namely, the magnitude of negative D_M, those two toroidicity-dominant equilibria and the two helicity-dominant equilibria produced qualitatively the same results, respectively. Therefore, thought to be quite reasonable are the categorization of the equilibria into toroidicity-dominant and helicity-dominant Mercier-unstable equilibria according to the degree of the reduction of the local magnetic shear by the Shafranov shift, and the resultant behavior of the pressure-driven modes in the both types of Mercier-unstable equilibria.

IV. CONCLUSION AND DISCUSSION

By means of global mode analysis of ideal MHD modes for Mercier-unstable equilibria in a planar axis $L = 2/M = 10$ heliotron/torsatron system with an inherently large Shafranov shift, the conjecture from

local mode analysis for Mercier-unstable equilibria[2] has been investigated and the properties of pressure-driven modes, namely, ballooning modes and interchange modes, inherent to such three-dimensional systems have been clarified.

From the viewpoint of the ideal MHD stability, a vacuum configuration of a planar axis $L = 2/M = 10$ heliotron/torsatron system is helicity-dominant, which comes from the helical coils. Both the local magnetic shear and normal magnetic curvature are mainly determined by helicity.[1,2] The characteristics of the finite-β equilibria in the planar axis $L = 2/M = 10$ heliotron/torsatron system are determined by an essentially axisymmetric large Shafranov shift.[1,2] The change in the local structures of the local magnetic shear (integrated along the magnetic field line) and the normal magnetic curvature by the Shafranov shift is related to toroidicity. The Shafranov shift reduces the (integrated) local magnetic shear on the outside of the torus, leading to the reduction of the field line bending stabilizing effect on ballooning modes. On the other hand, the Shafranov shift enhances (reduces) the local unfavorable normal magnetic curvature on the inner (outer) side of the torus.

According to the degree of the reduction of the local magnetic shear by the Shafranov shift, the Mercier-unstable equilibria in a planar axis $L = 2/M = 10$ heliotron/torsatron system can be categorized into two types, namely, toroidicity-dominant Mercier-unstable equilibria and helicity-dominant Mercier-unstable equilibria. The toroidicity-dominant Mercier-unstable equilibria are characterized by properties that the local magnetic shear is strongly reduced by a relatively large Shafranov shift, so that ballooning modes are easily destabilized. These equilibria are created with a peaked pressure profile either with zero net toroidal current or with net toroidal current such that the rotational transform increases slightly. The helicity-dominant Mercier-unstable equilibria are characterized by properties that the local magnetic shear is not reduced so much by a relatively small Shafranov shift, so that ballooning modes are not easily destabilized. These equilibria are created with a broad pressure profile with zero net toroidal current. The toroidicity-dominant Mercier-unstable equilibria tend to be more Mercier stable than the helicity-dominant Mercier-unstable equilibria, for the same β value at the magnetic axis, because the average magnetic curvature due to the Shafranov shift is favorable (unfavorable) in the region where the pressure gradient is large, for the former (latter) equilibria.

Since the local magnetic curvature due to helicity has the same period M in the toroidal direction as the toroidal field period of the equilibria, the characteristics of the pressure-driven modes in such Mercier-unstable equilibria dramatically change according to how much the local magnetic shear is reduced (whether the equilibrium is toroidicity-dominant or helicity-dominant) and also according to the relative magnitude of the typical toroidal mode numbers n of the perturbations compared with the toroidal field period M of the equilibria.

For the toroidicity-dominant Mercier-unstable equilibria, the pressure-driven modes change from interchange modes with negligible toroidal mode coupling for low toroidal mode numbers $n < M$, to tokamak-like poloidally localized ballooning modes with weak toroidal mode coupling for moderate toroidal mode numbers $n \sim M$, and finally to both poloidally and toroidally localized ballooning modes purely inherent to three-dimensional systems with strong poloidal and toroidal mode couplings for fairly high toroidal mode numbers $n \gg M$. Strong toroidal mode coupling, in cooperation with the poloidal mode coupling, makes the perturbation localize to flux tubes.

For the helicity-dominant Mercier-unstable equilibria, the pressure-driven modes change from interchange modes, with negligible toroidal mode coupling for $n < M$ or with weak toroidal mode

coupling for $n \sim M$, directly to poloidally and toroidally localized ballooning modes purely inherent to three-dimensional systems with strong poloidal and toroidal mode couplings for $n \gg M$.

Since the equilibria are Mercier unstable, interchange modes with low toroidal mode numbers $n < M$, experiencing the unfavorable magnetic curvature with its local structure averaged out, occur for both toroidicity-dominant and helicity-dominant equilibria. For fairly high toroidal mode numbers $n \gg M$, the perturbations can feel the fine local structure of the magnetic curvature due to helicity and also the local magnetic shear is reduced more or less in both types of equilibria, and consequently poloidally and toroidally localized ballooning modes inherent to three-dimensional systems are destabilized for both toroidicity-dominant and helicity-dominant Mercier-unstable equilibria. The situation for moderate toroidal mode numbers $n \sim M$ is different between toroidicity-dominant and helicity-dominant equilibria. The local magnetic shear is more reduced in toroidicity-dominant Mercier-unstable equilibria than in helicity-dominant Mercier-unstable equilibria, and also the modes with moderate toroidal mode numbers $n \sim M$ can not feel the local structure of the normal magnetic curvature due to helicity effectively. Thus, tokamak-like poloidally localized ballooning modes with a weak toroidal mode coupling can be easily destabilized for toroidicity-dominant Mercier-unstable equilibria, and interchange modes, driven by the average unfavorable magnetic curvature and not experiencing the effect of toroidal mode coupling, can be destabilized for helicity-dominant Mercier-unstable equilibria. Since the normal magnetic curvature becomes more unfavorable on the inner side of the torus than on the outer side of the torus by the Shafranov shift, the interchange modes are localized on the inner side of the torus for both types of equilibria. This type of interchange mode is anti-ballooning with respect to the poloidal mode coupling.

In both types of Mercier-unstable equilibria, the pressure-driven modes – ballooning modes and interchange modes – become more unstable and more localized both on flux tubes and in the radial direction, and have stronger toroidal mode coupling through the normal magnetic curvature due to helicity, as the typical toroidal mode numbers increase. Thus, we can expect that ballooning modes localized in one toroidal field period, as suggested in Ref. 2, may occur with very narrower radial extent and more unstable eigenvalues, as the typical toroidal mode numbers become larger and larger. All of these properties of the pressure-driven modes in two types of Mercier-unstable equilibria are quite consistent with the conjecture from local mode analysis given in Ref. 2.

For a particular MHD equilibrium, many unstable eigenmodes coexist, which comes from the difference of both the number of nodes in the radial direction and mode couplings in both the poloidal and toroidal directions. Since the interchange modes basically localize along mode rational magnetic field lines driven by the average favorable magnetic curvature, the toroidal mode coupling merely influences the localization in both the poloidal and toroidal directions but does not have an essential effect on the magnitude of the eigenvalues. This might have a possibility to lead to the existence of a narrow continuous unstable spectrum or a quasi-point unstable spectrum[3,11,12]. In contrast, the ballooning modes basically localize near the locally unfavorable magnetic curvature, so that toroidal mode coupling significantly influences the eigenvalues of the ballooning modes. Thus, ballooning modes in three-dimensional systems might be unable to have a continuous unstable spectrum or a quasi-point unstable spectrum, except perhaps for case with extremely high toroidal mode numbers $n \to \infty$.

In the Mercier-stable equilibria, only ballooning modes inherent to three-dimensional equilibria are expected from the local mode analysis[2]. These types

of equilibria usually have a shearless region, where the field line bending stabilizing effects are weak even for off-resonant modes, if the degree of the off-resonance is small. Also, the formalism of the high-mode-number ballooning modes breaks down there. Thus, the possibility for infernal modes[13] to occur must be investigated, which may determine the typical lowest toroidal mode numbers of the perturbation in the Mercier-stable equilibria. On the other hand, the typical highest toroidal mode numbers of the perturbation would be determined by kinetic effects, namely, the finite Larmor radius effects.

A detail analysis of a continuous unstable spectrum or a quasi-point unstable spectrum, and global mode analysis of Mercier-stable equilibria, and also the stabilizing effects due to the finite Larmor radius will be reported elsewhere.

ACKNOWLEDGMENTS

The authors express their gratitude to Professor T. Sato for his interest and encouragement. The calculations reported in this work were carried out on the SX supercomputer system of the National Institute for Fusion Science. The authors are also greatly indebted to Professor J. Nührenberg and Dr. C. Nührenberg for providing the CAS3D2MN code. Moreover, the authors would like to thank Professor J.W.Van Dam for fruitful discussions and his interest in this work.

One of the authors (J. Chen) was supported by the Japan Society for the Promotion of Science.

REFERENCES

[1] N. Nakajima, Phys. Plasmas **3**, 4545 (1996).

[2] N. Nakajima, Phys. Plasmas **3**, 4556 (1996).

[3] R.L. Dewar and A.H. Glasser, Phys. Fluids **26**, 3038 (1983).

[4] A. Iiyoshi, M. Fujiwara, O. Motojima, N. Oyabu, and K. Yamazaki, Fusion Technol. **17**, 148 (1990).

[5] S.P. Hirshman, Phys. Fluids **26**, 3553 (1983).

[6] A.H. Boozer. Phys. Fluids **23**, 904 (1980).

[7] C. Schwab. Phys. Fluids B **5**, 3195 (1993).

[8] C. Nührenberg. Phys. Plasmas **3**, 2401 (1996).

[9] J. Chen, N. Nakajima, and M. Okamoto, Comput. Phys. Commun. **113** 1 (1998).

[10] A.E. Lifschitz. in *Magnetohydrodynamics and Spectral Theory* (Kluwer Academic Publishers. Netherlands 1989), p.211

[11] W.A. Cooper. D.B. Singleton, and R.L. Dewar. Phys. Plasmas **3**, 275 (1996).

[12] P. Cuthbert, J.L.V. Lewandowski, H.J. Gardner. M. Persson. D.B. Singleton, R.L. Dewar, N. Nakajima, and W.A. Cooper, Phys. Plasmas **5**, 2921 (1998).

[13] J. Manickam, N. Pomphrey, and A.M.M. Todd. Nucl. Fusion **27**. 1461 (1987).

FIGURE CAPTIONS

Fig. 1 Schematic pictures of the level surfaces for unstable eigenvalues $\omega^2(<0)$ in (ψ, θ_k, α) space for (a) a Mercier-unstable three-dimensional equilibrium, and (b) a Mercier-stable three-dimensional equilibrium.

Fig. 2 Global rotational transform ι, global magnetic shear $s = 2\dfrac{d\ln\iota}{d\ln\psi}$, average magnetic curvature (average magnetic well or hill) index V'', and Mercier criterion parameter D_M, all as functions of the normalized minor radius $r_N = \sqrt{\psi_N}$. The upper (lower) graphs are for the toroidicity-dominant (helicity-dominant) Mercier-unstable equilibrium. For both equilibria, quantities corresponding to the vacuum configuration are drawn by dashed-and-dotted curves. Quantities drawn by dashed curves correspond to the modified equilibria mentioned in Sec. III C.

Fig. 3 (a) Equally spaced (ψ, θ) mesh, (b) contours of the local magnetic shear $\hat{s}$, and (c) the normal magnetic curvature multiplied by the Jacobian $\sqrt{g}\kappa^n$, on the vertically elongated (1st column) and horizontally elongated (2nd column) poloidal cross sections for the vacuum configuration. Thin (thick) curves in the contours of $\hat{s}$ indicate the negative (positive) region. Thin and thick curves in the contours of $\sqrt{g}\kappa^n$ indicate the locally unfavorable and locally favorable normal magnetic curvature regions, respectively. In the vacuum configuration, both the local magnetic shear and normal magnetic curvature are determined by helicity. The normal magnetic curvature is more unfavorable on the outside of the torus than on the inside of the torus.

Fig. 4 Same quantities as in Fig. 3 for the toroidicity-dominant Mercier-unstable equilibrium with a relatively large Shafranov shift. For each graph, the same contour level as one in Fig. 3 is used. Compared with the vacuum configuration shown in Fig. 3, the local magnetic shear is strongly reduced on the outer side of the torus, especially at the horizontally elongated poloidal cross section. Note that the Shafranov shift makes the normal magnetic curvature to be more unfavorable on the inside of the torus than on the outside of the torus.

Fig. 5 Same quantities as in Figs. 3 and 4 for the helicity-dominant Mercier-unstable equilibrium with a relatively small Shafranov shift. For each graph, the same contour level as one in Fig. 3 is used as well as in Fig. 4. Compared with the toroidicity-dominant Mercier-unstable equilibrium, the reduction of the local magnetic shear on the outer side of the torus is weaker. Just as in the toroidicity-dominant Mercier-unstable equilibrium, the normal magnetic curvature is more unfavorable on the inside of the torus than on the outside of the torus.

Fig. 6 (a) Plus signs denote the selected Fourier modes (m_e, n_e) from the Fourier space of the equilibrium, to make the perturbation together with the phase factor. Here, $M_{eq}^* = 186$ and the rectangular box $(-10 \le n_e/M \le 10,\ 0 \le m_e \le 30)$ indicates the Fourier space to construct the equilibrium. (b) Resultant Fourier modes of the perturbation (m, n), which are obtained according to Eq. (12) by using the selected Fourier modes (m_e, n_e) given in Fig. 6(a) and the phase factor $(M_p, N_p) = (38, 22)$. The broad plus sign shows the position of the phase factor, and the total number of the Fourier modes is $M_{pt} = 371$.

Fig. 7 Same quantities as in Fig. 6 for $M_{eq}^* = 336$ and $(M_p, N_p) = (133, 77)$. Thus, $M_{pt} = 671$.

Fig. 8 (a) Radial distribution of the Fourier components of the normal displacement $\vec{\xi}\cdot\nabla\psi$ with the dominant toroidal mode number, and the corresponding contours of the perturbed pressure $\tilde{P} = -\nabla P\cdot\vec{\xi}$ on the vertically (b) and horizontally (c) elongated poloidal cross sections. Here, $(M_p, N_p) = (5, 3)$, $M_{eq}^* = 76$, $M_{pt} = 151$, $N_S = 240$, $\Delta S = 4.2\times10^{-3}$, and $[\psi_N] = [0.08, 0.94]$. The eigenvalue is $\omega^2 = -4.99\times10^{-5}$.

Fig. 9 The same quantities as in Fig. 8 for $(M_p, N_p) = (38, 22)$, $M^*_{eq} = 186$, $M_{pt} = 371$, $N_S = 660$, $\Delta S = 1.5 \times 10^{-3}$, and $[\psi_N] = [0.1, 0.9]$, where the Fourier modes shown in Fig. 6 are used. There are three groups of Fourier modes with different toroidal mode numbers, and each group consists of Fourier modes with different poloidal mode numbers due to poloidal mode coupling. Here, the group with $n = 32$ is most dominant and the toroidal mode coupling is weak, leading to a tokamak-like poloidally localized ballooning mode. The eigenvalue is $\omega^2 = -1.89 \times 10^{-3}$, whose absolute value is larger than that in Fig. 8.

Fig. 10 (a) Radial distribution of the Fourier components of the normal displacement $\vec{\xi} \cdot \nabla\psi$ with the dominant toroidal mode numbers, and corresponding contours of the perturbed pressure $\tilde{P} = -\nabla P \cdot \vec{\xi}$ on the vertically (b) and horizontally (c) elongated poloidal cross sections, and (d) on the (θ, ζ) plane at $r_N = 0.734$. Here, $(M_p, N_p) = (342, 198)$, $M^*_{eq} = 397$, $M_{pt} = 793$, $N_S = 1840$, $\Delta S = 5.4 \times 10^{-4}$, and $[\psi_N] = [0.39, 0.66]$. The eight groups have different toroidal mode numbers and comparable magnitude, which leads to poloidally and toroidally localized ballooning structure. The outer side of the torus at the horizontally (vertically) elongated poloidal cross section is a locally unfavorable (favorable) curvature region; thus, the perturbed pressure existing on the outer side of the torus for the horizontally elongated poloidal cross section disappears on the outer side of the torus for the vertically elongated poloidal cross section. The eigenvalue is $\omega^2 = -6.32 \times 10^{-3}$, whose absolute value is larger than that in Fig. 9.

Fig. 11 (a) Radial distribution of the Fourier components of the normal displacement $\vec{\xi} \cdot \nabla\psi$ with their dominant toroidal mode numbers for the case when the origin of the poloidal angle is on the outer side of the torus. (b) Same quantity, when the origin of the poloidal angle is shifted from the outer side to the inner side of the torus in order to clarify the poloidal localization, and the corresponding contours of the perturbed pressure $\tilde{P} = -\nabla P \cdot \vec{\xi}$ on the vertically (c) and horizontally (d) elongated poloidal cross sections. Here, $(M_p, N_p) = (7, 4)$, $M^*_{eq} = 62$, $M_{pt} = 123$, $N_S = 300$, $\Delta S = 3.3 \times 10^{-3}$, and $[\psi_N] = [0.01, 0.98]$. The eigenvalue is $\omega^2 = -3.07 \times 10^{-3}$.

Fig. 12 The same quantities as in Fig. 9 for $(M_p, N_p) = (38, 22)$, $M^*_{eq} = 186$, $M_{pt} = 371$, $N_S = 660$, $\Delta S = 1.5 \times 10^{-3}$, and $[\psi_N] = [0.1, 0.9]$. The eigenvalue is $\omega^2 = -5.26 \times 10^{-3}$, whose absolute value is larger than that in Fig. 11.

Fig. 13 (a) Radial distribution of the Fourier components of the normal displacement $\vec{\xi} \cdot \nabla\psi$ with their dominant toroidal mode numbers for the case when the origin of the poloidal angle is on the outer side of the torus, and the corresponding contours of the perturbed pressure $\tilde{P} = -\nabla P \cdot \vec{\xi}$ on the vertically (b) and horizontally (c) elongated poloidal cross sections, and (d) on the (θ, ζ) plane at $r_N = 0.802$. Here, $(M_p, N_p) = (133, 77)$, $M^*_{eq} = 336$, $M_{pt} = 671$, $N_S = 1380$, $\Delta S = 7.2 \times 10^{-4}$, and $[\psi_N] = [0.36, 0.87]$. The eigenvalue is $\omega^2 = -6.39 \times 10^{-3}$, whose absolute value is larger than that in Fig. 12.

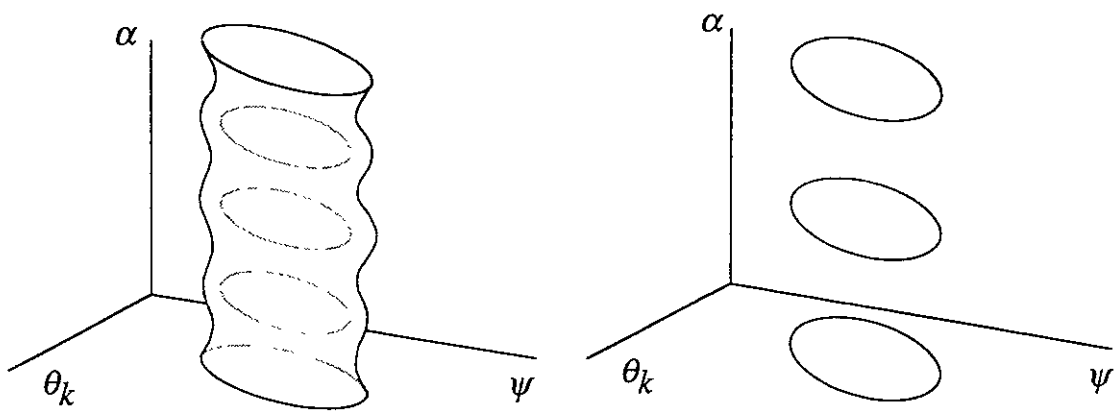

(a) (b)

Fig. 1, J.Chen et al.

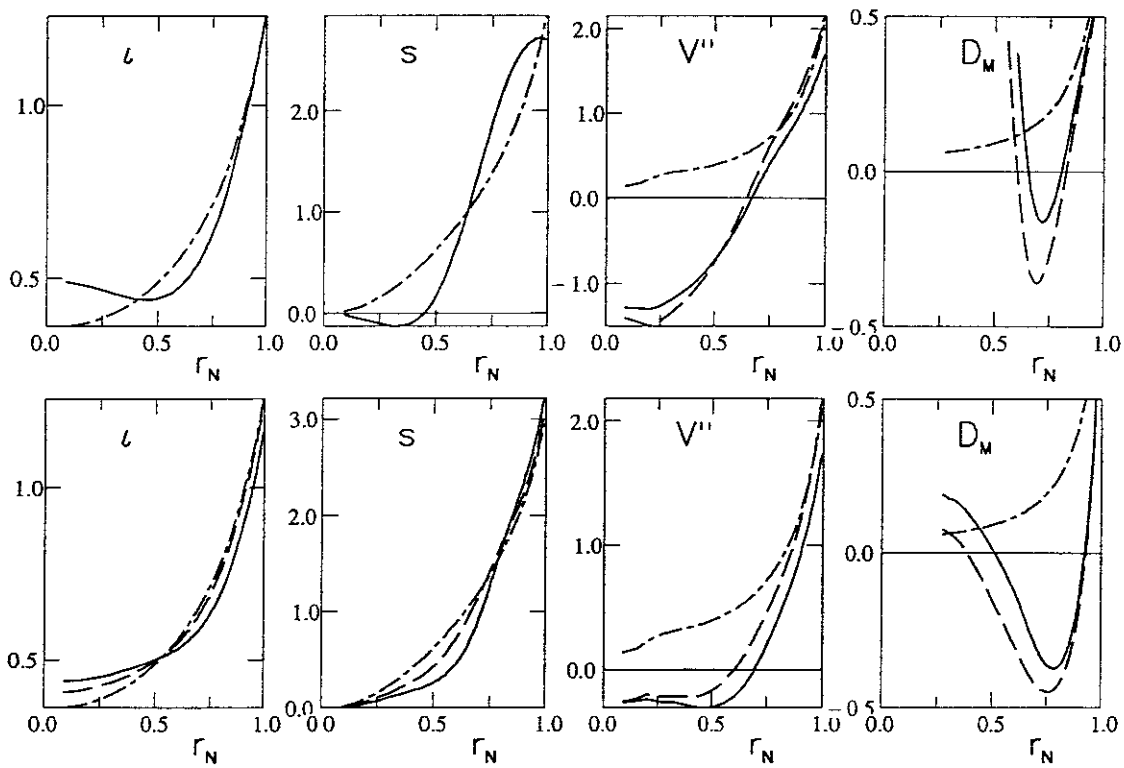

Fig. 2, J. Chen et al.

Fig. 3, J. Chen et al.

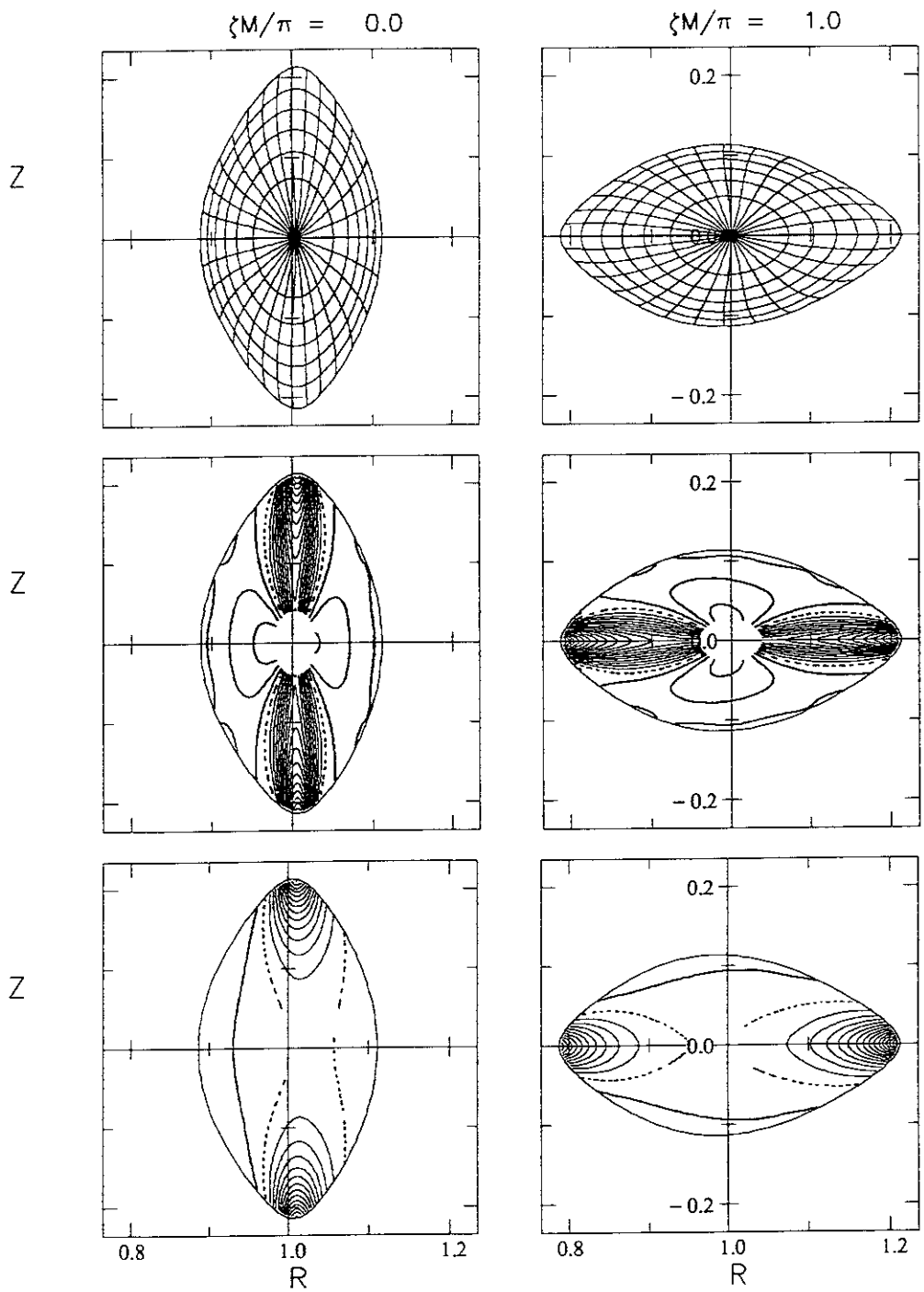

(a

(b

(c

Fig. 4, J. Chen et al.

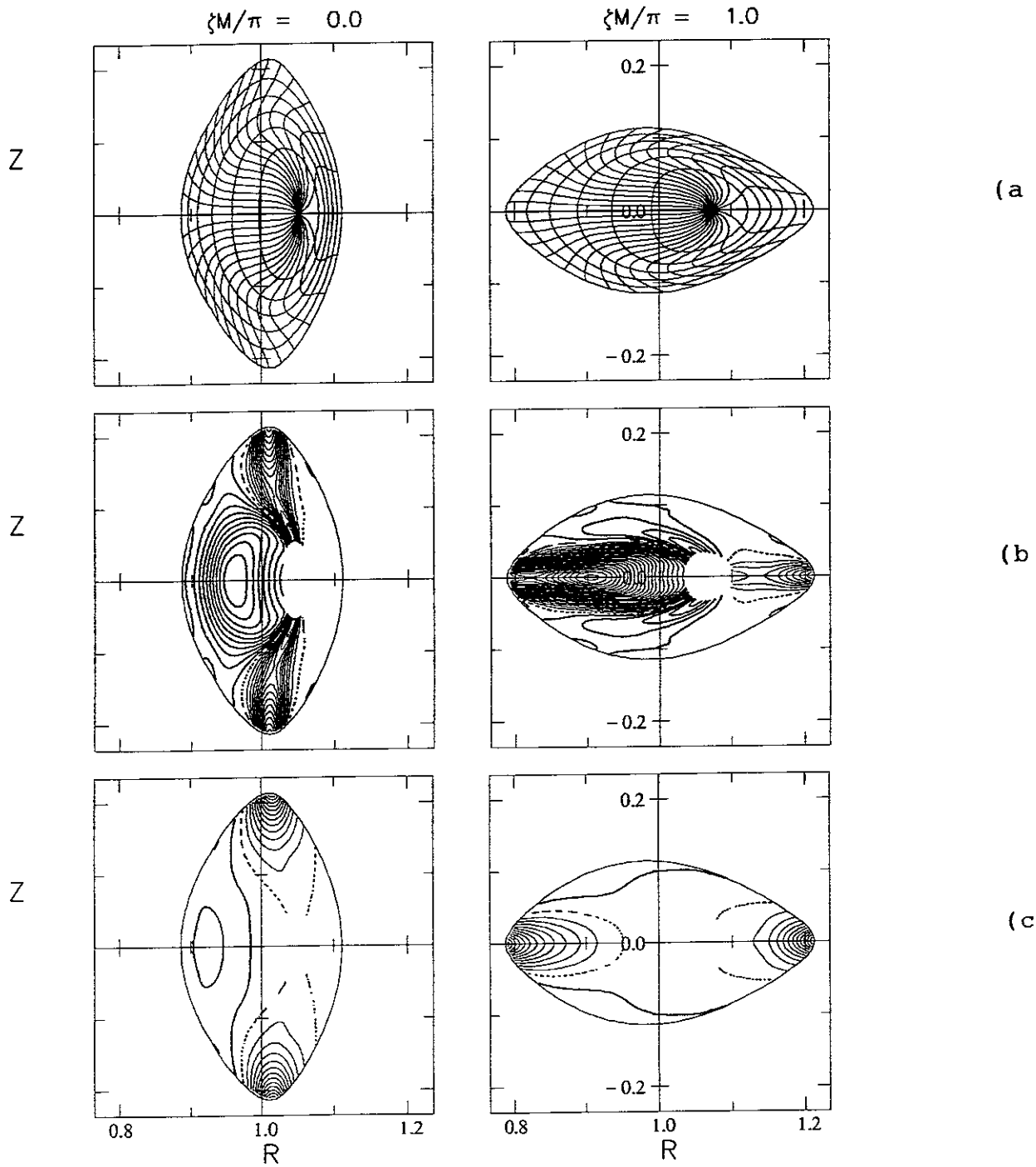

Fig. 5, J.Chen et al.

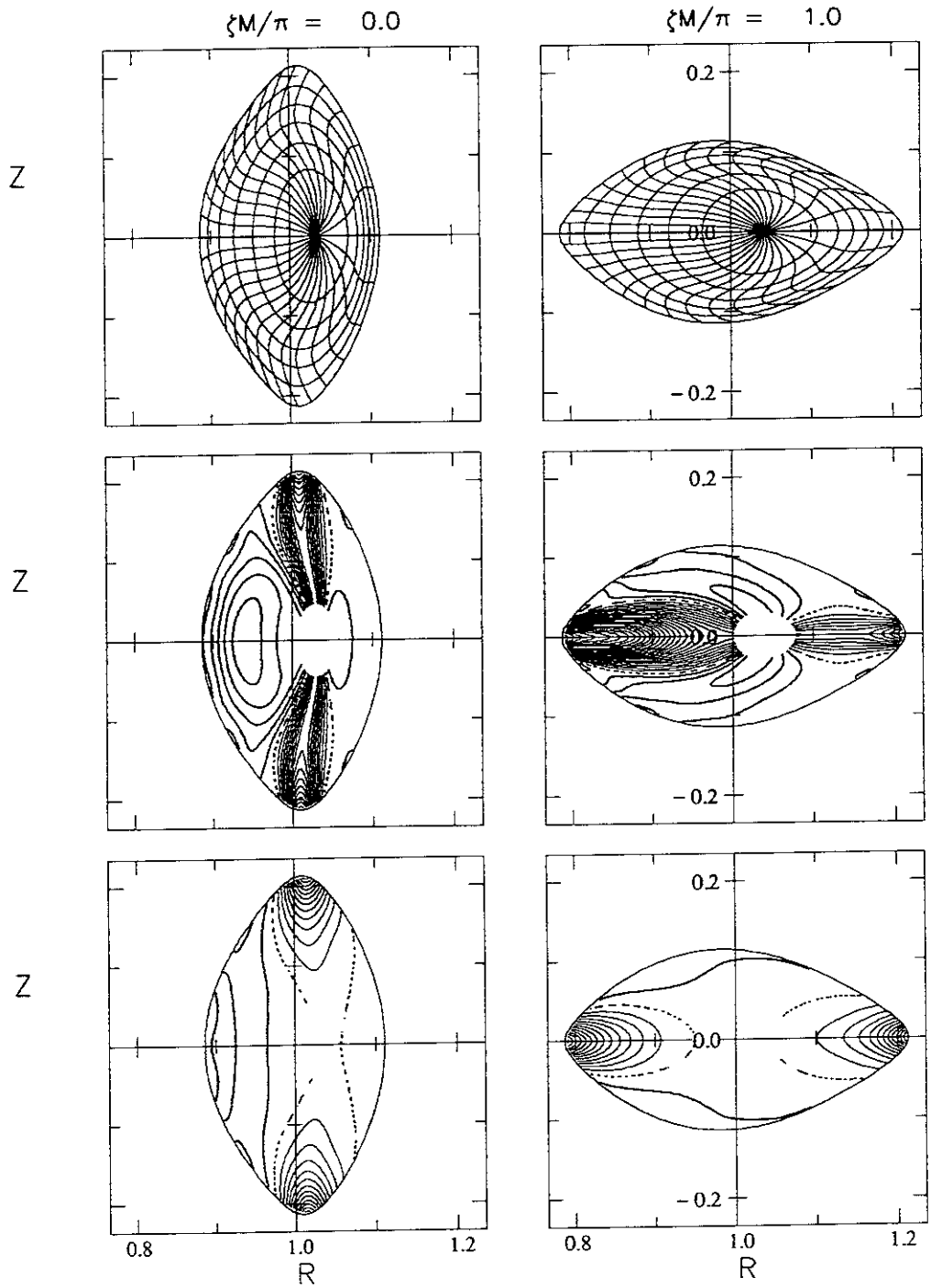

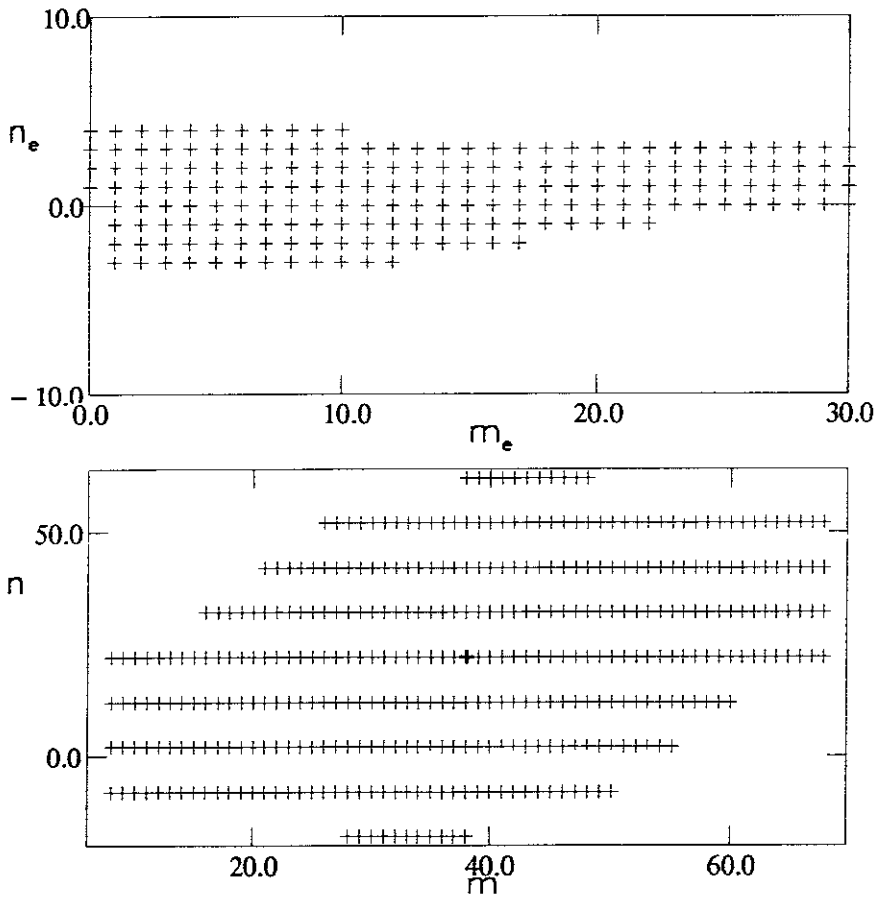

(a)

(b)

Fig. 6, J. Chen et al.

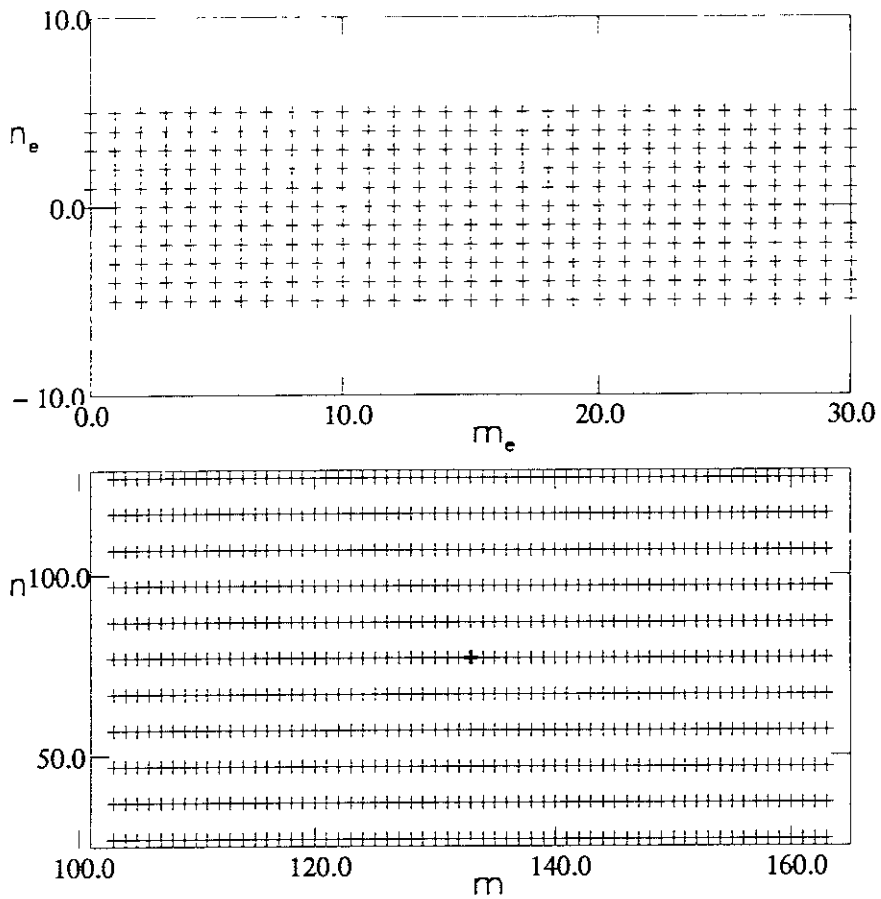

Fig. 7, J. Chen et al.

Fig. 8, J. Chen et al.

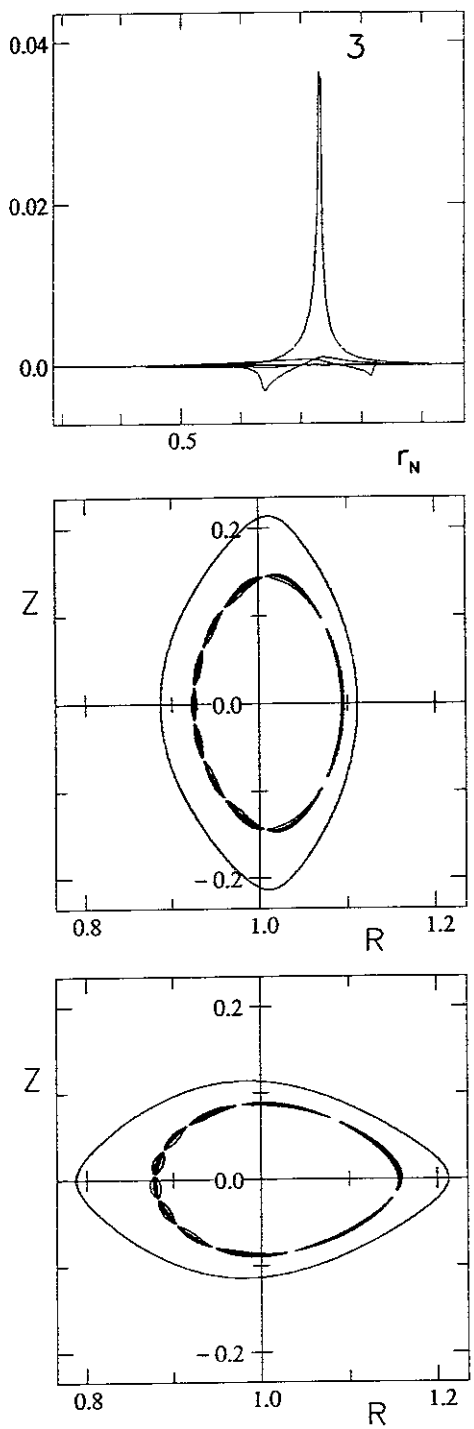

(a)

(b)

(c)

Fig. 9, Chen et al.

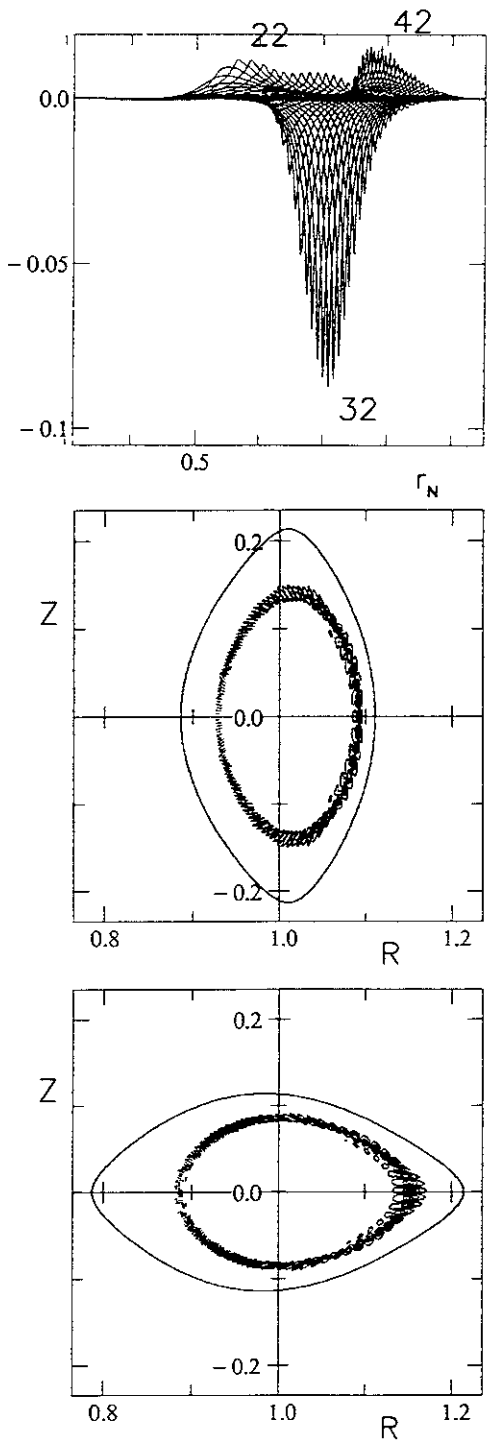

(a)

(b)

(c)

Fig. 10, J. Chen et al.

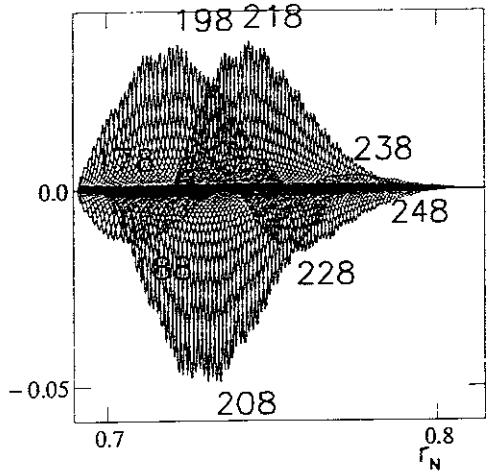

(a)

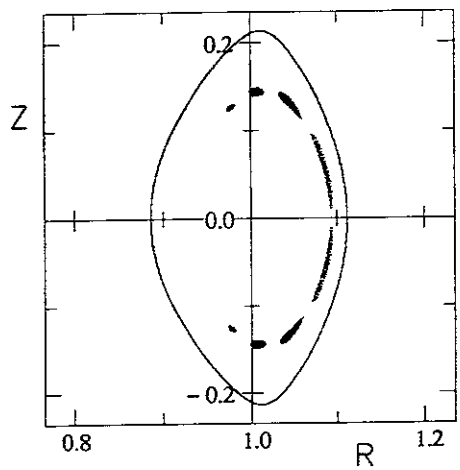

(b)

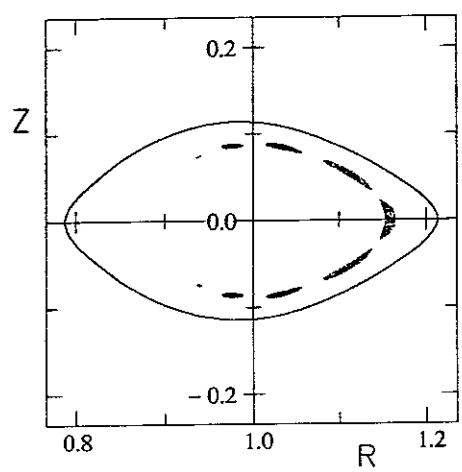

(c)

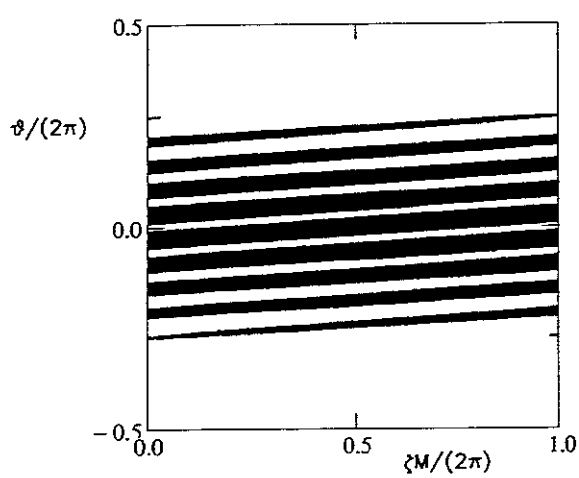

(d)

Fig. 11, J. Chen et al.

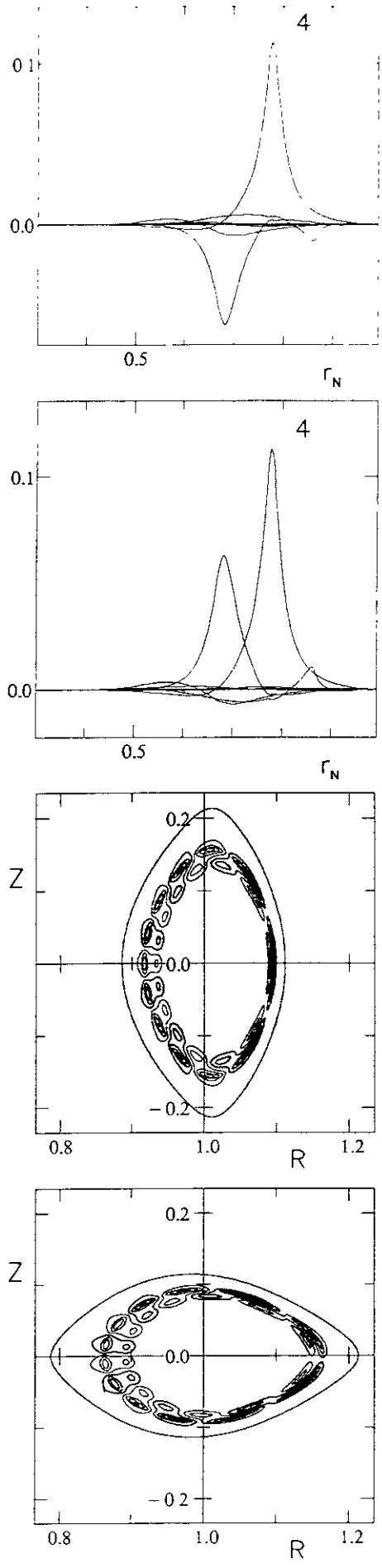

(a)

(b)

(c)

(d)

Fig. 12, J. Chen et al.

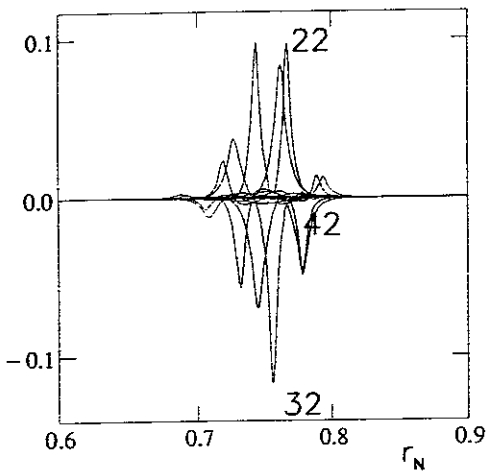

(a)

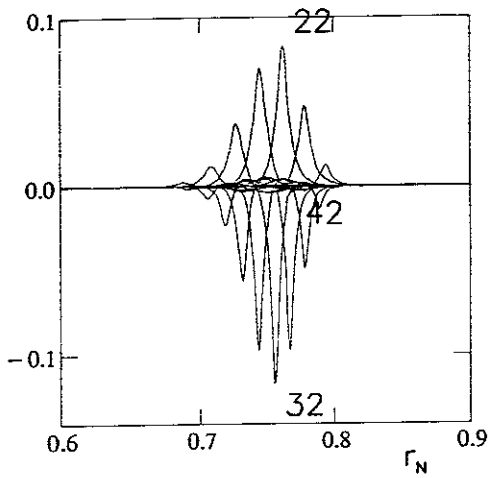

(b)

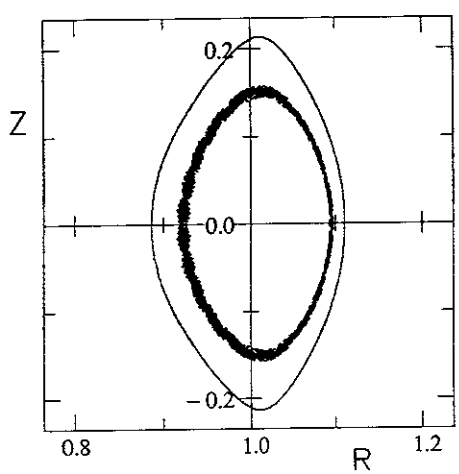

(c)

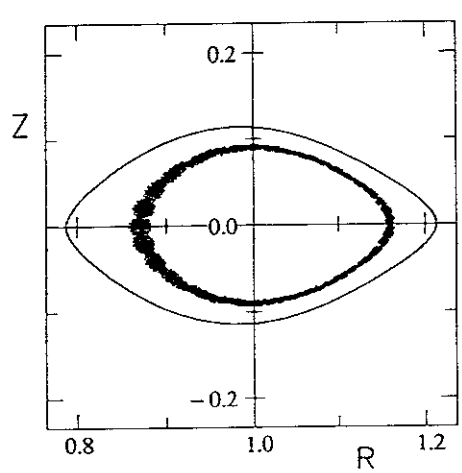

(d)

Fig. 13, J. Chen et al

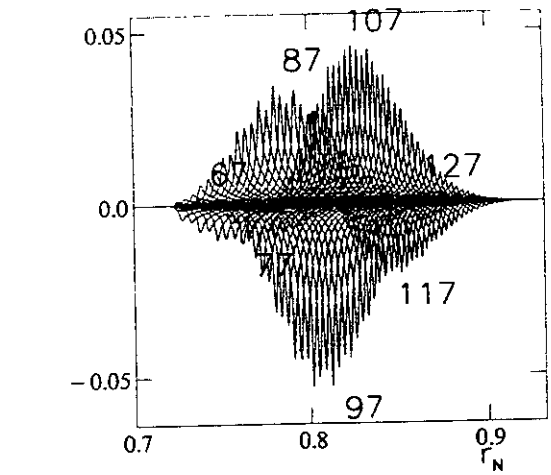

(a)

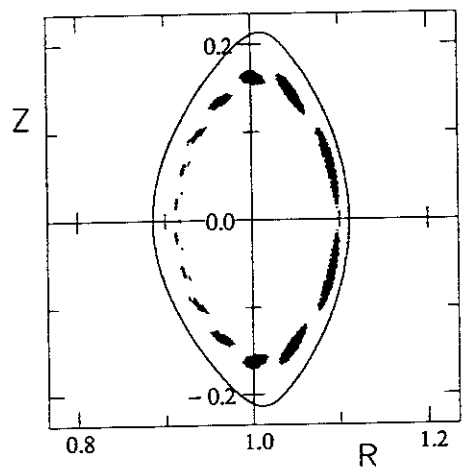

(b)

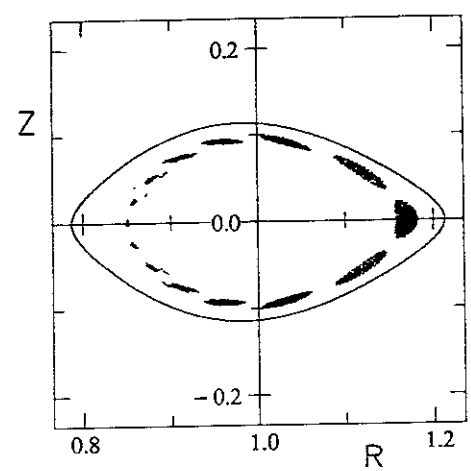

(c)

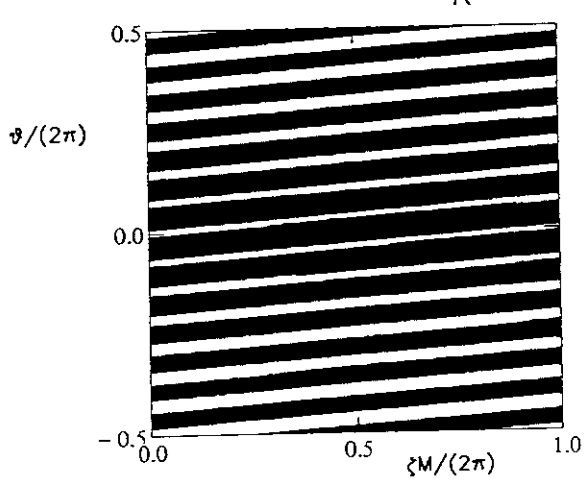

(d)

Recent Issues of NIFS Series

NIFS-516 *Papers Presented at the 6th H-mode Workshop (Seeon, Germany)*; Oct 1997

NIFS-517 John L. Johnson,
The Quest for Fusion Energy, Oct 1997

NIFS-518 J. Chen, N. Nakajima and M. Okamoto,
Shift-and-Inverse Lanczos Algorithm for Ideal MHD Stability Analysis, Nov 1997

NIFS-519 M. Yokoyama, N. Nakajima and M. Okamoto,
Nonlinear Incompressible Poloidal Viscosity in L=2 Heliotron and Quasi-Symmetric Stellarators, Nov 1997

NIFS-520 S. Kida and H. Miura
Identificaiton and Analysis of Vortical Structures, Nov 1997

NIFS-521 K. Ida, S. Nishimura, T. Minami, K. Tanaka, S. Okamura, M. Osakabe, H. Idei, S. Kubo, C. Takahashi and K. Matsuoka
High Ion Temperature Mode in CHS Heliotron/torsatron Plasmas, Nov 1997

NIFS-522 M. Yokoyama, N. Nakajima and M. Okamoto,
Realization and Classification of Symmetric Stellarator Configurations through Plasma Boundary Modulations, Dec. 1997

NIFS-523 H. Kitauchi,
Topological Structure of Magnetic Flux Lines Generated by Thermal Convection in a Rotating Spherical Shell, Dec 1997

NIFS-524 T. Ohkawa,
Tunneling Electron Trap; Dec 1997

NIFS-525 K. Itoh, S.-I. Itoh, M. Yagi, A. Fukuyama,
Solitary Radial Electric Field Structure in Tokamak Plasmas; Dec 1997

NIFS-526 Andrey N. Lyakhov,
Alfven Instabilities in FRC Plasma; Dec. 1997

NIFS-527 J. Uramoto,
Net Current Increment of negative Muonlike Particle Produced by the Electron and Positive Ion Bunch-method; Dec. 1997

NIFS-528 Andrey N. Lyakhov,
Comments on Electrostastic Drift Instabilities in Field Reversed Configuraiton; Dec. 1997

NIFS-529 J. Uramoto,
Pair Creation of Negative and Positive Pionlike (Muonlike) Particle by Interaction between an Electron Bunch and a Positive Ion Bunch; Dec. 1997

NIFS-530 J. Uramoto,
Measuring Method of Decay Time of Negative Muonlike Particle by Beam Collector Applied RF Bias Voltage; Dec. 1997

NIFS-531 J. Uramoto,
Confirmation Method for Metal Plate Penetration of Low Energy Negative Pionlike or Muonlike Particle Beam under Positive Ions; Dec 1997

NIFS-532 J. Uramoto,
Pair Creations of Negative and Positive Pionlike (Muonlike) Particle or K Mesonlike (Muonlike) Particle in H2 or D2 Gas Discharge in Magnetic Field, Dec 1997

NIFS-533 S. Kawata, C. Boonmee, T. Teramoto, L. Drska, J. Limpouch, R. Liska, M. Sinor,
Computer-Assisted Particle-in-Cell Code Development; Dec 1997

NIFS-534 Y. Matsukawa, T. Suda, S. Ohnuki and C. Namba,
Microstructure and Mechanical Property of Neutron Irradiated TiNi Shape Memory Alloy, Jan. 1998

NIFS-535 A. Fujisawa, H. Iguchi, H. Idei, S. Kubo, K. Matsuoka, S. Okamura, K. Tanaka, T. Minami, S. Ohdachi, S. Morita, H Zushi, S. Lee, M. Osakabe, R. Akiyama, Y. Yoshimura, K. Toi, H. Sanuki, K. Itoh, A. Shimizu, S. Takagi, A. Ejiri, C. Takahashi, M. Kojima, S. Hidekuma, K. Ida, S. Nishimura, N. Inoue, R. Sakamoto, S.-I. Itoh, Y. Hamada, M. Fujiwara,
Discovery of Electric Pulsation in a Toroidal Helical Plasma; Jan. 1998

NIFS-536 Lj.R. Hadzievski, M.M. Skoric, M. Kono and T Sato,
Simulation of Weak and Strong Langmuir Collapse Regimes; Jan. 1998

NIFS-537 H. Sugama, W. Horton,
Nonlinear Electromagnetic Gyrokinetic Equation for Plasmas with Large Mean Flows, Feb 1998

NIFS-538 H. Iguchi, T.P. Crowley, A. Fujisawa, S. Lee, K. Tanaka, T. Minami, S. Nishimura, K. Ida, R. Akiyama, Y. Hamada, H., Idei, M. Isobe, M. Kojima, S. Kubo, S. Monta, S. Ohdachi, S. Okamura, M. Osakabe, K. Matsuoka, C. Takahashi and K Toi,
Space Potential Fluctuations during MHD Activities in the Compact Helical System (CHS); Feb 1998

NIFS-539 Takashi Yabe and Yan Zhang,
Effect of Ambient Gas on Three-Dimensional Breakup in Coronet Formation Process, Feb. 1998

NIFS-540 H. Nakamura, K. Ikeda and S. Yamaguchi,
Transport Coefficients of InSb in a Strong Magnetic Field; Feb. 1998

NIFS-541 J. Uramoto,
Development of ν_μ Beam Detector and Large Area ν_μ Beam Source by H_2 Gas Discharge (I); Mar 1998

NIFS-542 J. Uramoto,
Development of $bar\{\nu\}_\mu$ Beam Detector and Large Area $bar\{\nu\}_\mu$ Beam Source by H_2 Gas Discharge (II), Mar 1998

NIFS-543 J. Uramoto,
Some Problems inside a Mass Analyzer for Pions Extracted from a H_2 Gas Discharge; Mar 1998

NIFS-544 J. Uramoto,
Simplified ν_μ, $bar\{\nu\}_\mu$ Beam Detector and ν_μ, $bar\{\nu\}_\mu$ Beam Source by Interaction between an Electron Bunch and a Positive Ion Bunch; Mar. 1998

NIFS-545 J. Uramoto,
Various Neutrino Beams Generated by D_2 Gas Discharge; Mar.1998

NIFS-546 R. Kanno, N. Nakajima, T. Hayashi and M Okamoto,
Computational Study of Three Dimensional Equilibria with the Bootstrap Current, Mar. 1998

NIFS-547 R. Kanno, N. Nakajima and M. Okamoto,
Electron Heat Transport in a Self-Similar Structure of Magnetic Islands; Apr. 1998

NIFS-548 J.E. Rice,
Simulated Impurity Transport in LHD from MIST; May 1998

NIFS-549 M.M. Skoric, T. Sato, A.M. Maluckov and M S Jovanovic,
On Kinetic Complexity in a Three-Wave Interaction; June 1998

NIFS-550 S. Goto and S Kida,
Passive Scalar Spectrum in Isotropic Turbulence: Prediction by the Lagrangian Direct-interaction Approximation; June 1998

NIFS-551 T. Kuroda, H. Sugama, R. Kanno, M. Okamoto and W. Horton,
Initial Value Problem of the Toroidal Ion Temperature Gradient Mode ; June 1998

NIFS-552 T. Mutoh, R. Kumazawa, T. Seki, F. Simpo, G. Nomura, T. Ido and T. Watari,
Steady State Tests of High Voltage Ceramic Feedthoughs and Co-Axial Transmission Line of ICRF Heating System for the Large Helical Device ; June 1998

NIFS-553 N Noda, K Tsuzuki, A Sagara, N Inoue, T Muroga,
oronization in Future Devices -Protecting Layer against Tritium and Energetic Neutrals-, July 1998

NIFS-554 S. Murakami and H Saleem,
Electromagnetic Effects on Rippling Instability and Tokamak Edge Fluctuations, July 1998

NIFS-555 H Nakamura, K Ikeda and S Yamaguchi,
Physical Model of Nernst Element, Aug 1998

NIFS-556 H. Okumura, S Yamaguchi, H Nakamura, K Ikeda and K Sawada,
Numerical Computation of Thermoelectric and Thermomagnetic Effects; Aug 1998

NIFS-557 Y. Takein, M. Osakabe, K Tsumon, Y Oka, O Kaneko, E Asano, T Kawamoto, R. Akıyama and M Tanaka,
Development of a High-Current Hydrogen-Negative Ion Source for LHD-NBI System; Aug.1998

NIFS-558 M. Tanaka, A. Yu Grosberg and T Tanaka,
Molecular Dynamics of Structure Organization of Polyampholytes; Sep. 1998

NIFS-559 R. Horiuchi, K. Nishimura and T. Watanabe,
Kinetic Stabilization of Tilt Disruption in Field-Reversed Configurations, Sep 1998
(IAEA-CN-69/THP1/11)

NIFS-560 S. Sudo, K. Kholopenkov, K. Matsuoka, S Okamura, C. Takahashi, R. Akiyama, A. Fujisawa, K. Ida, H Idei, H Iguchi, M Isobe, S. Kado, K Kondo, S Kubo, H. Kuramoto, T. Minami, S Morita, S Nishimura, M. Osakabe, M. Sasao, B Peterson K. Tanaka, K Toi and Y. Yoshimura,
Particle Transport Study with Tracer-Encapsulated Solid Pellet Injection, Oct 1998
(IAEA-CN-69/EXP1/18)

NIFS-561 A Fujisawa, H. Iguchi, S Lee, K Tanaka, T Minami, Y. Yoshimura, M Osakabe, K Matsuoka, S. Okamura, H Idei, S. Kubo S Ohdachi, S Morita, R Akiyama, K Toi, H Sanuki, K Itoh, K. Ida, A Shimizu, S Takagi, C Takahashi, M Kojima, S Hidekuma, S Nishimura, M. Isobe, A Ejiri, N Inoue, R Sakamoto, Y. Hamada and M Fujiwara,
Dynamic Behavior Associated with Electric Field Transitions in CHS Heliotron/Torsatron, Oct 1998
(IAEA-CN-69/EX5/1)

NIFS-562 S. Yoshikawa,
Next Generation Toroidal Devices; Oct 1998

NIFS-563 Y Todo and T Sato,
Kinetic-Magnetohydrodynamic Simulation Study of Fast Ions and Toroidal Alfvén Eigenmodes, Oct 1998
(IAEA-CN-69/THP2/22)

NIFS-564 T Watari, T Shimozuma, Y. Takeiri, R. Kumazawa, T Mutoh, M. Sato, O Kaneko, K Ohkubo, S. Kubo, H Idei Y. Oka, M Osakabe, T. Seki, K. Tsumori, Y Yoshimura, R. Akiyama, T Kawamoto, S. Kobayashi, F Shimpo, Y Takita, E. Asano, S. Itoh G Nomura, T. Ido, M. Hamabe, M Fujiwara, A Iiyoshi, S. Morimoto, T. Bigelow and Y P. Zhao,
Steady State Heating Technology Development for LHD, Oct 1998
(IAEA-CN-69/FTP/21)

NIFS-565 A. Sagara, K.Y. Watanabe, K. Yamazaki, O. Motojima, M Fujiwara, O. Mitarai, S Imagawa, H Yamanishi, H. Chikaraishi, A Kohyama, H. Matsui, T Muroga, T. Noda, N Ohyabu, T. Satow, A.A. Shishkin, S Tanaka, T. Terai and T Uda,
LHD-Type Compact Helical Reactors, Oct 1998
(IAEA-CN-69/FTP/03(R)

NIFS-566 N. Nakajima, J. Chen, K Ichiguchi and M Okamoto,
Global Mode Analysis of Ideal MHD Modes in L=2 Heliotron/Torsatron Systems, Oct 1998
(IAEA-CN-69/THP1/08)

NIFS-567 K Ida, M. Osakabe, K. Tanaka, T Minami, S Nishimura, S Okamura, A. Fujisawa, Y Yoshimura, S Kubo, R Akiyama, D S Darrow, H Idei, H Iguchi, M. Isobe, S Kado, T. Kondo, S Lee, K Matsuoka, S Morita, I Nomura, S Ohdachi, M Sasao, A Shimizu, K. Tumori, S. Takayama, M. Takechi, S. Takagi, C Takahashi, K Toi and T. Watari,
Transition from L Mode to High Ion Temperature Mode in CHS Heliotron/Torsatron Plasmas, Oct 1998
(IAEA-CN-69/EX2/2)

NIFS-568 S Okamura, K. Matsuoka, R Akiyama, D.S. Darrow, A Ejiri, A Fujisawa, M Fujiwara, M Goto, K Ida H Idei, H Iguchi, N Inoue M Isobe, K. Itoh, S Kado, K Khlopenkov, T. Kondo, S. Kubo, A Lazaros, S Lee, G. Matsunaga, T. Minami, S. Morita, S Murakami, N Nakajima, N Nikai, S. Nishimura, I. Nomura, S. Ohdachi, K Ohkuni, M. Osakabe, R. Pavlichenko, B Peterson, R Sakamoto, H. Sanuki, M Sasao, A Shimizu, Y Shirai, S Sudo, S. Takagi, C Takahashi, S. Takayama, M Takechi, K. Tanaka, K Toi, K. Yamazaki, Y. Yoshimura and T Watari,
Confinement Physics Study in a Small Low-Aspect-Ratio Helical Device CHS; Oct 1998
(IAEA-CN-69/OV4/5)

NIFS-569 M.M. Skoric, T. Sato, A Maluckov, M.S. Jovanovic,
Micro- and Macro-scale Self-organization in a Dissipative Plasma;Oct 1998

NIFS-570 T. Hayashi, N. Mizuguchi, T-H Watanabe, T. Sato and the Complexity Simulation Group,
Nonlinear Simulations of Internal Reconnection Event in Spherical Tokamak;Oct 1998
(IAEA-CN-69/TH3/3)

NIFS-571 A. Iiyoshi, A. Komori, A Ejiri, M. Emoto, H. Funaba, M. Goto, K. Ida, H. Idei, S. Inagaki, S. Kado, O. Kaneko, K Kawahata, S Kubo, R. Kumazawa, S Masuzaki, T. Minami, J. Miyazawa, T. Morisaki, S. Morita, S Murakami, S. Muto, T Muto, Y Nagayama, Y. Nakamura, H Nakanishi, K. Narihara, K. Nishimura, N Noda, T. Kobuchi, S Ohdachi, N Ohyabu, Y. Oka, M Osakabe, T. Ozaki, B.J. Peterson, A. Sagara, S. Sakakibara, R Sakamoto, H. Sasao, M. Sasao, K. Sato, M. Sato, T. Seki, T Shimozuma, M. Shoji, H. Suzuki, Y. Takeiri, K Tanaka, K Toi, T. Tokuzawa, K. Tsumori, I. Yamada, H. Yamada, S. Yamaguchi, M. Yokoyama K.Y.Watanabe, T. Watari, R. Akiyama, H. Chikaraishi, K. Haba, S. Hamaguchi, S. Iima, S. Imagawa, N. Inoue, K. Iwamoto, S. Kitagawa, Y. Kubota, J. Kodaira, R. Maekawa, T. Mito. T. Nagasaka, A. Nishimura, Y. Takita, C. Takahashi, K. Takahata, K. Yamauchi, H. Tamura, T Tsuzuki, S. Yamada, N. Yanagi, H. Yonezu, Y. Hamada, K. Matsuoka, K. Murai, K. Ohkubo, I Ohtake, M. Okamoto, S. Sato, T. Satow, S. Sudo, S Tanahashi, K Yamazaki, M. Fujiwara and O Motojima,
An Overview of the Large Helical Device Project; Oct 1998
(IAEA-CN-69/OV1/4)

NIFS-572 M. Fujiwara, H. Yamada, A. Ejiri, M. Emoto, H. Funaba, M. Goto, K. Ida, H. Idei, S. Inagaki, S. Kado, O. Kaneko, K. Kawahata, A. Komori, S. Kubo, R. Kumazawa, S. Masuzaki, T. Minami, J. Miyazawa, T. Morisaki, S. Morita, S Murakami, S. Muto, T. Muto, Y. Nagayama, Y. Nakamura, H. Nakanishi, K. Narihara, K. Nishimura, N. Noda, T. Kobuchi, S Ohdachi, N. Ohyabu, Y. Oka, M. Osakabe, T. Ozaki, B. J. Peterson, A. Sagara, S Sakakibara, R Sakamoto, H. Sasao, M. Sasao, K. Sato, M. Sato, T. Seki, T Shimozuma, M. Shoji, H. Sazuki, Y. Takeiri, K. Tanaka, K. Toi, T Tokuzawa, K. Tsumori, I. Yamada, S Yamaguchi, M. Yokoyama, K.Y. Watanabe, T. Watari, R. Akiyama, H. Chikaraishi, K. Haba, S. Hamaguchi, M Iima, S. Imagawa, N Inoue, K. Iwamoto, S. Kitagawa, Y. Kubota, J. Kodaira, R. Maekawa, T Mito, T. Nagasaka, A Nishimura, Y. Takita, C Takahashi, K. Takahata, K. Yamauchi, H. Tamura, T. Tsuzuki, S. Yamada, N Yanagi, H Yonezu, Y. Hamada, K. Matsuoka, K. Murai, K Ohkubo, I. Ohtake, M Okamoto, S. Sato, T Satow, S Sudo, S Tanahashi, K Yamazaki, O Motojima and A. Iiyoshi,
Plasma Confinement Studies in LHD; Oct 1998
(IAEA-CN-69/EX2/3)

NIFS-573 O. Motojima, K Akaishi, H. Chikaraishi, H Funaba, S Hamaguchi, S Imagawa, S Inagaki, N. Inoue, A. Iwamoto, S. Kitagawa, A. Komori, Y. Kubota, R. Maekawa, S. Masuzaki, T. Mito, J. Miyazawa, T Morisaki, T Muroga, T Nagasaka, Y Nakmura, A. Nishimura, K Nishimura, N. Noda, N. Ohyabu, S. Sagara, S Sakakibara, R. Sakamoto, S. Satoh, T. Satow, M Shoji, H Suzuki, K. Takahata, H. Tamura, K. Watanabe, H Yamada, S. Yamada, S. Yamaguchi, K. Yamazaki, N. Yanagi, T. Baba, H. Hayashi, M. Iima, T. Inoue, S. Kato, T. Kato, T. Kondo, S. Moriuchi, H. Ogawa, I. Ohtake, K. Ooba, H. Sekiguchi, N. Suzuki, S. Takami, Y. Taniguchi, T Tsuzuki, N. Yamamoto, K. Yasui, H. Yonezu, M. Fujiwara and A. Iiyoshi,
Progress Summary of LHD Engineering Design and Construction; Oct. 1998
(IAEA-CN-69/FT2/1)

NIFS-574 K. Toi, M. Takechi, S. Takagi, G. Matsunaga, M. Isobe, T. Kondo, M. Sasao, D.S. Darrow, K. Ohkuni, S. Ohdachi, R. Akiyama A. Fujisawa, M. Gotoh, H. Idei, K. Ida, H. Iguchi, S. Kado, M. Kojima, S. Kubo, S. Lee, K. Matsuoka, T. Minami, S. Morita. N. Nikai, S. Nishimura, S. Okamura, M Osakabe, A. Shimizu, Y. Shirai, C. Takahashi, K. Tanaka, T. Watari and Y. Yoshimura,
Global MHD Modes Excited by Energetic Ions in Heliotron/Torsatron Plasmas,Oct. 1998
(IAEA-CN-69/EXP1/19)

NIFS-575 Y. Hamada, A. Nishizawa, Y. Kawasumi, A. Fujisawa, M. Kojima, K. Narihara, K. Ida, A. Ejiri, S. Ohdachi, K Kawahata, K Toi, K. Sato, T. Seki, H. Iguchi, K. Adachi, S. Hidekuma, S.Hirokura, K. Iwasaki, T. Ido, R. Kumazawa, H. Kuramoto. T. Minami, I.. Nomura, M. Sasao, K.N. Sato, T. Tsuzuki, I. Yamada and T. Watari,
Potential Turbulence in Tokamak Plasmas;Oct. 1998
(IAEA-CN-69/EXP2/14)

NIFS-576 S. Murakami, U. Gasparino, H. Idei, S. Kubo, H Maassberg, N Marushchenko, N. Nakajima, M Romé and M. Okamoto,
5D Simulation Study of Suprathermal Electron Transport in Non-Axisymmetric Plasmas,Oct 1998
(IAEA-CN-69/THP1/01)

NIFS-577 S Fujiwara and T. Sato,
Molecular Dynamics Simulation of Structure Formation of Short Chain Molecules. Nov. 1998

NIFS-578 T. Yamagishi,
Eigenfunctions for Vlasov Equation in Multi-species Plasmas Nov 1998

NIFS-579 M. Tanaka, A. Yu Grosberg and T Tanaka,
Molecular Dynamics of Strongly-Coupled Multichain Coulomb Polymers in Pure and Salt Aqueous Solutions;Nov. 1998

NIFS-580 J. Chen, N. Nakajima and M. Okamoto,
Global Mode Analysis of Ideal MHD Modes in a Heliotron/Torsatron System: I. Mercier-unstable Equilibria; Dec. 1998